

The Pennsylvania State University  
The Graduate School

**ANALYSIS OF A HEAVY PRECIPITATION EVENT DURING “PRE”-CIP  
USING REGIONAL AND GLOBAL MODEL FORECASTS**

A Thesis in  
Meteorology and Atmospheric Science  
by  
Andreas C. Sandino

© 2023 Andreas C. Sandino

Submitted in Partial Fulfillment  
of the Requirements  
for the Degree of

Master of Science

December 2023

The thesis of Andreas C. Sandino was reviewed and approved by the following:

Anthony C. Didlake Jr.  
Associate Professor of Meteorology  
Thesis Advisor

Yunji Zhang  
Assistant Professor of Meteorology

Jose D. Fuentes  
Professor of Meteorology and Atmospheric Science

Jan-Huey Chen  
Scientist at NOAA GFDL  
Special Signatory

Paul Markowski  
Department Head and Distinguished Professor of Meteorology

# Abstract

Extreme rainfall events are high-impact weather phenomena that are often difficult to predict because fundamental processes forcing such events are not yet fully understood. This study focuses on a heavy precipitation summertime convection event that produced a mesoscale convective vortex (MCV) in northeastern Colorado using radar observations, the NOAA GFDL C-SHiELD global model, and the PSU WRF-EnKF regional ensemble model. These datasets allowed for a comprehensive examination of the essential features and processes needed to generate this specific event, an inter-model comparison across a hierarchy of models, and an assessment of the predictability of this and similar events. The selected C-SHiELD forecast best matched the observed conditions and accurately simulated an MCV. The WRF ensemble simulations were categorized into three distinct groups: ‘similar to obs’, ‘backheavy’, and ‘simulated MCV’. The ‘similar to obs’ group differed notably from the other two WRF groups due to the absence of midlevel moisture, which increased dry air entrainment rates and limited the duration and amount of precipitation. The other two WRF groups, characterized by more moist environments, stronger updrafts, and the presence of moderate wind shear, contributed to sustained convection, resulting in an overestimation of precipitation. The study also highlighted the contrasting performance of the WRF and C-SHiELD models, with the WRF model showing greater fidelity in capturing the event’s characteristics. Overall, this research contributes to a better understanding of convective precipitation forecasting and underscores the need for cautious interpretation of model outputs, along with potential future applications in ensemble forecasting endeavors.

# Table of Contents

<b>List of Figures</b>	<b>vi</b>
<b>Acknowledgments</b>	<b>ix</b>
<b>Chapter 1</b>	
<b>Introduction</b>	<b>1</b>
<b>Chapter 2</b>	
<b>Data and Methods</b>	<b>5</b>
2.1 Background . . . . .	5
2.2 SHIELD Model . . . . .	5
2.3 PSU WRF-EnKF . . . . .	7
2.4 MRMS and StageIV . . . . .	7
<b>Chapter 3</b>	
<b>Event Overview and Simulation Selection</b>	<b>10</b>
3.1 Storm Overview . . . . .	10
3.2 C-SHIELD simulation selection . . . . .	13
3.3 PSU WRF-EnKF ensemble grouping . . . . .	15
<b>Chapter 4</b>	
<b>Results</b>	<b>21</b>
4.1 Thermodynamic Assessment . . . . .	21
4.2 Representative Group Soundings . . . . .	25
4.3 Reflectivity CFADs . . . . .	28
4.4 Vertical Velocity and Vertical Moisture Flux CFADs . . . . .	31
4.5 Convective-to-Stratiform Life Cycle . . . . .	33
<b>Chapter 5</b>	
<b>Conclusions</b>	<b>38</b>



# List of Figures

2.1	C-SHiELD configuration. The cubed-sphere edges are shown as thick black lines, and the nested grid over the continental U.S. is shown within red. Gray lines outside the red mesh show the model grid boxes, where the horizontal grid spacing is 13 km for the global domain and 3 km for the nested domain. . . . .	6
2.2	(a) Model domains utilized in the PSU WRF-EnKF simulations for this case. The 9 km (outer) and 3 km (inner) domains are delineated by blue boxes, while the red box indicates the specific region analyzed. All precipitation analyses are conducted within the red circle, while all other analyses are performed within the red rectangle. (b) Zoomed-in view of the 3 km domain. The same red circle from (a) is centered on the green dot, which is the location of the CSU-CHILL radar. . . . .	8
3.1	(a-c) Composite MRMS reflectivity (in dBZ) at 16 MDT 30 July, 21 MDT 30 July, and 01 MDT 31 July. These three specific time points represented by the MRMS reflectivity will remain consistent throughout this case study. The red rectangle is the same as a red rectangle from the previous figure. (d) 1-Day rain accumulation (mm) from StageIV observations between 6 MDT 30 July and 6 MDT 31 July. . . . .	12
3.2	Hourly precipitation accumulations from the six C-SHiELD model forecasts (initialization times and forecast lead times in legend) and StageIV observations. Thick red line represents the selected C-SHiELD 36-hour forecast. The grey background after 21 MDT corresponds to nighttime in late July. The black vertical dashed lines are at 16, 21, and 01 MDT. . . . .	13
3.3	(a-c) Composite reflectivity plan views at 16 MDT, 21 MDT, and 01 MDT for the C-SHiELD 36-hour forecast. The red square represents our domain of interest. (d-f) Same as (a)-(c) but for PSU WRF-EnKF ensemble member #18. . . . .	16

3.4	Hovmöller diagrams of 2-km average reflectivity (dBZ) for the (a) MRMS, (b) C-SHiELD 36-hour forecast, and (c) PSU WRF-EnKF ensemble #18. Reflectivity is averaged over the y dimension and shown as a function of x distance and time. The average is taken from the square rectangular domain from FIG 3.3. Black dashed lines denote 16 MDT, 21 MDT, and 01 MDT. . . . .	17
3.5	Hourly precipitation accumulations of the individual WRF ensemble members divided into three groups: (a) ‘Similar to obs’, (b) ‘Backheavy’ and (c) ‘Simulated MCV’ groups. The Stage IV observations and C-SHiELD 36-hr forecast accumulations are shown in black and red thick lines. The grey background corresponds to nighttime. Time points consistent from before are marked by vertical dashed lines. The color of each group indicated in the legend will remain consistent for future analyses. . . . .	18
3.6	Left-hand column: Composite plan views of reflectivity from the 4 ensemble members of the ‘simulated MCV’ group at select times. Dashed lines indicate the locations of west-east vertical cross-sections for each ensemble member. Right-hand column: Vertical cross sections depicting: PV (shaded in $10^{-5} \text{ m}^2 \text{ s}^{-1} \text{ K}^{-1} \text{ kg}^{-1}$ ), potential temperature (theta; red contours every 3K) and relative humidity (60% and 90% dashed lines). . . . .	19
4.1	Time series depicting the evolution of (a) CAPE, (b) CIN, (c) 500 hPa PV, (d) 4 km specific humidity, (e) 4 km vertical velocity, and (f) 4 km vertical moisture flux (VMF) within the square domain of interest for C-SHiELD and each averaged WRF group. Analysis time points still indicated by dashed vertical lines, and the grey background corresponds to nighttime. . . . .	23
4.2	Histograms of CAPE (top row) and CIN (bottom row) domain averages from each model group. Evaluation times align with the previous time selections. Frequencies are normalized by the number of grid points within the domain. . . . .	24
4.3	Observational soundings from (a) CSU Radiosonde and (b-c) NWS Denver at select times during the event. . . . .	26
4.4	Soundings shown for one representative ensemble member in each group at 16 MDT, 21 MDT, and 01 MDT. Row (a) shows an ensemble member #4 from the ‘similar to obs’, (b) is #15 from the ‘backheavy’ group, and (c) is #3 from the ‘simulated MCV’ group. . . . .	27
4.5	Reflectivity CFADs for each WRF group at 16 MDT (left), 21 MDT (middle) and 01 MDT (right). Reflectivity CFADs were binned every 2 dB and normalized by the maximum frequency at each time. . . . .	29

4.6	Top row shows the same CFADs from ‘similar to obs’ group in Fig. 4.5. Second and third rows show reflectivity CFAD difference plots at the same times. Red colors represent higher frequencies compared to the ‘similar to obs’ group, and blue colors portray lower frequencies than the ‘similar to obs’ group. . . . .	30
4.7	Vertical velocity CFADs for each WRF group at 16 MDT (left), 21 MDT (middle) and 01 MDT (right). Velocity CFADs were binned every 0.5 m/s. The Contour colorbar is on an exponential scale. Frequencies above $10^3$ are excluded to highlight the relatively lower occurrences of higher vertical velocity values. . . . .	32
4.8	Top row shows the same CFADs from ‘similar to obs’ group in Fig. 4.7. Second and third rows show vertical velocity CFAD difference plots at the same times. Red colors represent higher frequencies compared to the ‘similar to obs’ group, and blue colors portray lower frequencies than the ‘similar to obs’ group. . . . .	33
4.9	As in Figure 4.7, but for vertical moisture flux (VMF). VMF frequencies were binned every $0.002 \text{ kg m}^{-2} \text{ s}^{-1}$ . . . . .	34
4.10	As in Figure 4.8, but for VMF. . . . .	35
4.11	Vertical mass transport (VMT) profiles for each group at select times. Positive (red), Negative (blue), and Net (black) VMT profiles for each group at analysis times. VMT profiles are normalized by the maximum positive VMT. . . . .	36

# Acknowledgments

I would like to express my sincere gratitude to my advisor, Anthony Didlake, for his invaluable guidance and support during my research at Penn State. His expertise and mentorship have been instrumental in shaping my work on this captivating subject. I am also immensely grateful to Jose Fuentes, Jo-Anne Manswell Butty, Charles Ichoku, and other members of the NOAA Center for Atmospheric Science and Meteorology (NCAS-M) for providing me with the opportunity to intern at the Geophysical Fluid Dynamics Laboratory (GFDL). Their unwavering support and encouragement have been invaluable in enriching my research experience. I am deeply thankful to Jan-Huey Chen, Ming-Jing Tong, and other employees at GFDL for their remarkable kindness and adaptability in assisting me with navigating the C-SHiELD model output during the initial stages of this study. Their expertise and assistance have been invaluable in shaping the direction of my research. I would also like to extend my appreciation to my committee members, Jan-Huey Chen, Yunji Zhang and Jose Fuentes for their valuable input and perspectives on this thesis. Their feedback and suggestions have significantly enriched the quality of my work. I am also grateful to my friends and colleagues in meteorology for their support and camaraderie throughout this journey. Lastly, I would like to express my heartfelt thanks to my family for their unwavering support and encouragement in my lifelong pursuit of knowledge.

This work was made possible thanks to the National Science Foundation (NSF) and the NCAS-M Award No. NA16SEC48100006. The views expressed in this publication are solely those of the author(s) and do not necessarily reflect the views of the NSF or NCAS-M.

# Chapter 1

## Introduction

Heavy precipitation events have a profound impact on communities worldwide, yet our current understanding and ability to accurately forecast these rainfall events remain limited. The consequences of heavy precipitation and flash flooding are felt regardless of geographic location. However, it is important to recognize that the thresholds for defining "extreme" or "heavy" precipitation can vary across regions, leading to different impacts from similar precipitation amounts. These events pose significant risk to property, and sometimes cause major damage and financial loss (Pielke and Downton, 2000; Trigg et al., 2016; Klotzbach et al., 2018). In 2021, global flood damages amounted to approximately \$60 billion, with over 1,800 reported fatalities, followed by \$35 billion in damages and over 5,000 reported fatalities the following year (Centre for Research on the Epidemiology of Disasters (CRAD), 2021, 2022). Despite advancements in numerical weather prediction that have improved event simulation accuracy, opportunities for further enhancements persist. Understanding the underlying mechanisms driving such phenomena is of utmost importance, given the escalating frequency and severity of them globally (Bronstert, 2003; Hirabayashi et al., 2013; Wing et al., 2018; Dougherty and Rasmussen, 2020).

By delving deeper into the complex dynamics of heavy precipitation events and their associated risk, we can enhance our understanding and predictive capabilities despite their occurrence in diverse climates. They range from the moisture-rich western North Pacific to comparatively drier regions like the northern Colorado plains, presenting formidable challenges. To address these scientific and forecasting challenges, the Prediction of Rainfall Extremes Campaign In the Pacific (PRECIP) was established. This comprehensive research campaign (set to take place in Taiwan and Japan) aimed to investigate the mechanisms governing extreme rainfall and enhance predictive modeling techniques. Both Taiwan and Japan provide exceptional research environments with

abundant moisture, complex terrain, oceanic conditions, and robust operational networks. The insights gained from this campaign would also be transferable to diverse weather phenomena, including those impacting the United States. Originally planned for 2020, the project extended into a three-year endeavor due to the impact of COVID-19. To align with the broader project framework and to prepare for the Taiwan/Japan portion of the campaign (given the practical limitations from COVID-19 restrictions), the Preparatory Rockies Experiment for the Campaign In the Pacific ("PRE"-CIP) was conducted in 2021. This preliminary campaign utilized a comprehensive approach, integrating modeling and observational techniques with the Pennsylvania State University (PSU) Weather Research and Forecasting (WRF) Ensemble Kalman Filter (PSU WRF-EnKF) system over the continental US (CONUS) and northern Colorado. The observational network for this campaign included radiosondes for environmental profiling, Micro Pulse dialers for monitoring atmospheric moisture, and three Doppler radars: Colorado State University's CHIVO and CHILL (CSU-CHIVO and CSU-CHILL) and the National Center for Atmospheric Research (NCAR) S-Pol. By investigating the drier environment of northern Colorado, this campaign provided a valuable point of comparison with the moisture-rich northwestern Pacific, leading to insights into the fundamental mechanisms behind heavy rainfall in diverse environments.

The presence of the Rocky Mountains in Colorado notably shapes local weather patterns, with two prominent orographic features playing a crucial role. The first feature is the north-south Front Range, which abruptly rises 2 km from the High Plains. The second feature is a west-east ridge expanding eastward from the central Rockies (Dirks, 1969). These orographic features, combined with the prevailing influence of a substantial climatological anticyclone at 500 mb during the summer, establish a circulation pattern that promotes upward motions over the mountain range, impacting storm development in the region (Lopez and Holle, 1986). This interaction between the topography and atmospheric circulation facilitates enhanced ascent that sometimes contribute to the formation of storms. Furthermore, the forecast for convection initiation (CI) relies on the convergence of essential ingredients, including moisture, instability, and a lifting mechanism, all of which are critical for the development of convective cells (Doswell, 1986). Previous studies in Colorado have also identified localized topographic areas often referred to as "hot spots", that serve as focal points for the organization and initiation of convective processes (Henz, 1973; Karr and Wooten, 1976; Riley et al., 1987).

According to Fritsch et al. (1986), Mesoscale Convective Systems (MCSs) account

for approximately 30%–70% of warm-season (April–September) precipitation between the Rocky Mountains and the Mississippi River. These MCSs typically originate over the Rockies and propagate eastward, inducing low level convergence and contributing to the nocturnal maximum of precipitation between the areas (Dai et al., 1999). As a result of their association with intense and prolonged rainfall, MCSs frequently give rise to flash flooding events (Junker et al., 1999; Moore et al., 2003; Gochis et al., 2015). The precipitation rate is influenced by moisture, vertical motions, and precipitation efficiency (Doswell et al., 1996). Several studies have categorized flash floods into one of four types: synoptic, frontal, meso-high or western. They have also highlighted the role of various ingredients, such as strong low level winds, moisture advection, and frontal boundaries in influencing flooding patterns (Maddox et al., 1999; Junker et al., 1999). Moreover, while mesoscale convective vortices (MCVs) are not always associated with MCSs, they sometimes form within these systems and play a role in their development (Bartels and Maddox, 1991; Knievel, 2001). These rotating features in the atmosphere can intensify and sustain convective activity, leading to enhanced precipitation (Bosart and Sanders, 1981; Zhang and Fritsch, 1987; Fritsch et al., 1994; Trier and Davis, 2002; Schumacher and Johnson, 2009; Schumacher et al., 2013).

MCS prediction relies on its representation in forecast models, using either global or regional modeling approaches. Global models excel in simulating synoptic and global-scale conditions, but their mesoscale convective precipitation forecasts are limited due to reliance on convective parameterizations at coarse grid-scales. Since accurately representing convection is crucial for the proper simulation of extreme precipitation events, modern mesoscale models have reduced their reliance on convective parameterizations (on their finest grid meshes) due to their impacts on simulation and forecast errors (Done et al., 2004; Weisman et al., 2013). This so-called "convective-allowing" approach explicitly simulates convection circulations, and would theoretically produce better simulations with sufficiently small grid spacing. Other model assumptions and microphysical parameterizations may also contribute to overall error (Morrison et al., 2020b). Another weather modeling tool is an ensemble prediction system, which generates multiple forecasts to effectively communicate forecast uncertainty. This is unlike deterministic forecasts that only have one output (Demeritt et al., 2007). Although the skill displayed in deterministic forecasts increases as lead time shortens, certain drawbacks remain such as their incomplete assessments of forecast variability (Yang et al., 2021). Multiple studies regarding ensemble forecasting have highlighted both successful predictions

and limitations in modeling convection. In the past decade, there have been notable improvements in the capabilities of ensemble forecasts to deliver accurate precipitation predictions and storm structure (Wheatley et al., 2015; Schwartz et al., 2015; Jones et al., 2016; Flora et al., 2019; Galarneau et al., 2022). However, challenges persist as most models still cannot resolve many of properties associated with convective updrafts and stratiform processes (Bryan et al., 2003). Part of the “PRE”-CIP campaign motivation was to address these modeling deficiencies by using high-resolution mesoscale and global models to improve understanding of precipitation processes.

This study aims to examine the critical processes necessary for one heavy summertime convective precipitation event in northeastern Colorado, and its predictability using multiple numerical models. Additionally, we aim to identify important dynamic, thermodynamic, and kinematic processes necessary for CI and storm maintenance. By analyzing a specific event associated with an observed MCV during the 2021 “PRE”-CIP campaign, we seek to enhance our understanding of the underlying processes leading to such phenomena through an inter-model comparison. Notably, both the PSU WRF-EnKF and the National Oceanic and Atmospheric Administration (NOAA) Geophysical Fluid Dynamics Laboratory (GFDL) Continental System for High Resolution Prediction on Earth to Local Domains (C-SHiELD) models are “convection-allowing”. To continue driving improvements, it is imperative to examine and assess the performance of models across a wide range of weather phenomena. In this context, our ultimate goal is to present an assessment in the ability of a hierarchy of “convective-allowing” models to accurately simulate the selected event, and to understand the key processes that drove the variability in the simulations.

Chapter 2 will cover the data and methods used in this study. Chapter 3 will present an overview of this summertime convective precipitation event and initial model analyses. The results will be discussed in chapter 4. Finally, the conclusions will be presented in chapter 5.

# Chapter 2

## Data and Methods

### 2.1 Background

The objective of this research is to analyze the critical ingredients need for the formation and intensification of an MCS that lasted between 06 MDT 30 July to 06 MDT 31 July 2021 (local time) in northeastern Colorado. This chapter will provide a comprehensive overview of the data collection methods and analysis techniques employed for this study, with special emphasis on the utilization of both regional and global model forecasts. Analysis primarily involves the evaluation of model simulations by comparison against radar-estimated precipitation amounts, with the aim of assessing overall model performance and the ability to capture the observed precipitation patterns.

### 2.2 SHiELD Model

The National Oceanic and Atmospheric Administration (NOAA) Geophysical Fluid Dynamics Laboratory (GFDL) recently developed the innovative SHiELD global model. This model offers enhanced flexibility and accuracy in global simulations by combining the non-hydrostatic Finite-Volume Cubed-Sphere Dynamical Core (FV3; Harris and Lin, 2013; Lin, 2004; Putman and Lin, 2007; Harris et al., 2021) with model physics schemes from the National Centers for Environmental Prediction's (NCEP) operational forecasting model, the Global Forecasting System (Harris et al., 2020). The SHiELD model includes five distinct configurations, one of which is the Continental SHiELD (C-SHiELD), specifically designed for modeling convection and predicting severe weather events across the CONUS. The model supports a variety of spatial and temporal scales,

with specific emphasis on short-to-medium range and subseasonal-to-seasonal weather forecasting. The model grid used is displayed in Figure 2.1. The C-SHiELD configuration employs the NCEP scale-aware Simplified Arakawa-Schubert convection scheme (Han et al., 2017), which includes both shallow and deep convection. It also uses both the five-category GFDL microphysics and cloud fraction scheme (Zhou, 2019) and a scale-aware TKE-EDMF Planetary Boundary Layer (PBL) scheme (Han and Bretherton, 2019). However, the application of the deep convection scheme in the C-SHiELD model is limited to the global domain, while the convection scheme is disabled for the 3 km domain (GFDL, 2021). It uses a global cubed-sphere grid with a 13 km horizontal grid spacing that includes a 3 km nest over the CONUS and 63 Lagrangian vertical levels. Each face along the global domain contains  $768 \times 768$  grid cells (C768 grid), rotated and unstretched to a width of 9 km over the CONUS, enabling the benefits of the integrated modeling approach. The model is initialized twice daily (00Z and 12Z) from operational GFS analyses. For the event of interest, six C-SHiELD model runs with different initialization times were examined in further detail.

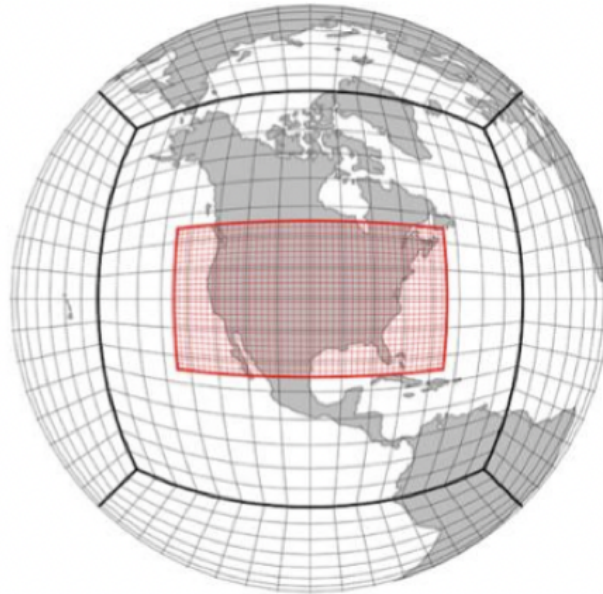


**Figure 2.1.** C-SHiELD configuration. The cubed-sphere edges are shown as thick black lines, and the nested grid over the continental U.S. is shown within red. Gray lines outside the red mesh show the model grid boxes, where the horizontal grid spacing is 13 km for the global domain and 3 km for the nested domain.

## 2.3 PSU WRF-EnKF

The PSU WRF-EnKF (hereafter referred to as WRF) is a state-of-the-art data assimilation and forecast model that has been developed and used for studying a variety of weather phenomena (Zhang et al., 2009, 2011b; Zhang and Weng, 2015; Zhang et al., 2016a, 2011a; Weng and Zhang, 2012b,a; Chen and Zhang, 2019; Chan et al., 2020; Zhang et al., 2021). The model combines the ensemble square root filter data assimilation scheme (Whitaker and Hamill, 2002) with the fully compressible, mesoscale WRF model (Skamarock et al., 2005) that incorporates non-hydrostatic effects using an Arakawa-C grid (Bernardet, 1995). To simulate weather systems at high resolution and capture convective processes, the model domain is tailored to the area of interest. For the 2021 “PRE”-CIP campaign, two one-way nested domains were chosen. The first, with a horizontal grid spacing of 9 km ( $400 \times 320 \times 50$ ), covers the western CONUS, while the second, a 3 km domain ( $390 \times 30 \times 50$ ), covers Colorado and neighboring states (Figure 2.2a). Both domains contain 50 vertical levels and use the Thompson microphysics scheme, MYNN surface and planetary boundary layer physics, and no cumulus parameterizations for both domains (Zhang et al., 2023). The boundary conditions for WRF are generated using the same initial conditions for the Global Ensemble Forecast System. After 3 hours of ensemble spin up, the system undergoes 9 hours of data assimilation using conventional (including surface and sounding) observations, and all-sky infrared brightness temperatures from channel 10 of the Advanced Baseline Imager onboard the GOES-16 satellite. After data assimilation, 48-hour forecast simulations are produced using a 40 and 20-member ensemble with hourly output.

## 2.4 MRMS and StageIV

Two operational datasets were utilized to conduct a quantitative and spatial evaluation of precipitation predicted by global and regional model forecasts. The first dataset is the Multi-Radar/Multi-Sensor (MRMS) system (Zhang et al., 2016b), which integrates over 180 operational WSR-88D radars, satellite, and surface/upper-air observations to generate advanced radar products, such as composite reflectivity. The resulting gridded data is outputted hourly with a horizontal grid spacing of  $0.01^\circ \times 0.01^\circ$  (or approximately 1km), covering the CONUS. We use the composite reflectivity to validate the reflectivity outputs from both models. The second operational dataset is the StageIV precipitation product

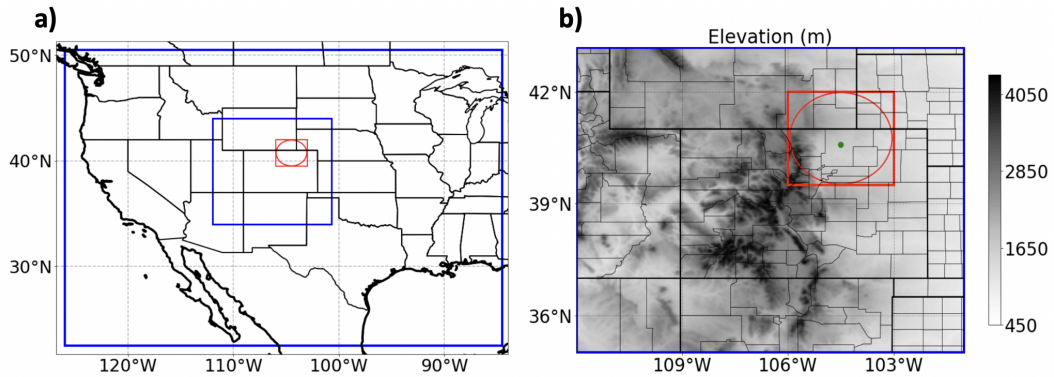


**Figure 2.2.** (a) Model domains utilized in the PSU WRF-EnKF simulations for this case. The 9 km (outer) and 3 km (inner) domains are delineated by blue boxes, while the red box indicates the specific region analyzed. All precipitation analyses are conducted within the red circle, while all other analyses are performed within the red rectangle. (b) Zoomed-in view of the 3 km domain. The same red circle from (a) is centered on the green dot, which is the location of the CSU-CHILL radar.

(Nelson et al., 2016), which is a near-real-time product produced by NCEP and the National Weather Service (NWS). Such observations provide estimates of precipitation on a  $4 \times 4 \text{ km}^2$  grid over the CONUS based on a combination of radar and rain gauge data. StageIV was employed to verify the simulated precipitation accumulations throughout the event’s lifetime.

In our analysis of both the observational datasets and the simulation output, we focused within the  $330 \times 280 \text{ km}$  rectangular domain shown in red in Fig. 2.2b. This domain, spanning  $106^\circ\text{W}$  to  $103^\circ\text{W}$  longitude and  $39.5^\circ\text{N}$  to  $42^\circ\text{N}$  latitude, captures the area most affected by heavy rainfall. To capture precipitation processes occurring near the topographical features, the western half of our domain encompasses the Front Range and the foothills of the Rockies. This decision was based on CI along the foothills, and the extension of convective processes across the entire domain, including areas further east. The selected domain played a central role in conducting the majority of our research analyses, excluding those related to precipitation accumulation and sounding profile plots. In particular, precipitation data from the StageIV rain product and the C-SHiELD and PSU WRF-EnKF models utilized a circular region of interest (with 140 km radius) that encompassed the CSU-CHILL radar (refer to Figure 2.2b). The choice of a circular geometry for precipitation comparisons takes into consideration the potential utilization of CSU-CHILL precipitation data in future research. This would facilitate additional analysis using another observational dataset, thereby providing valuable insights into the

accuracy of both model output.

# Chapter 3

## Event Overview and Simulation Selection

### 3.1 Storm Overview

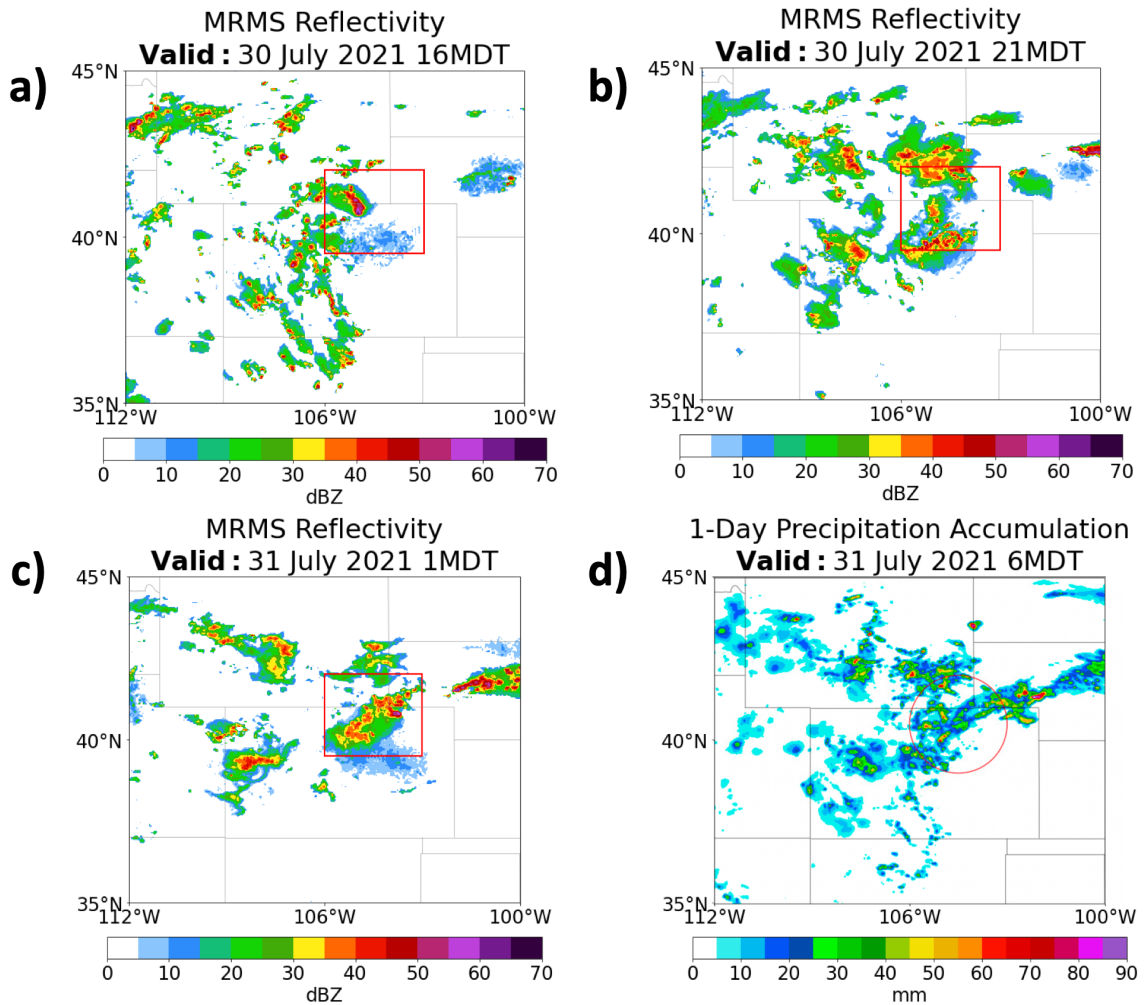
A typical summertime thunderstorm developed in northeastern Colorado that triggered an hour-long flash flood warning from 2340-0040 MDT on 30-31 July 2021. By examining this case study, we aim to shed light on the complex interactions between synoptic-scale and mesoscale features that resulted in localized heavy rainfall and flash flooding. Although heavy precipitation was observed during this event, it was nominal in the sense that it was not very widespread. Due to the limited selection of events resulting from predetermined radar deployment dates, we chose this event characterized by the presence of an MCV and the issuance of a flash flood warning. According to the NWS Boulder forecast discussion, the storm developed within the context of a weak north to northeast flow, coinciding with the progression of a strong cold front moving southeast into south-central Wyoming and Colorado's Front Range. Notably, the presence of moisture-rich air in the mid- to upper-levels of the atmosphere further contributed to the formation and intensification of this weather system. This section provides an overview of the background synoptic-scale environment and precipitation evolution of the storm.

At 02 MDT 30 July (08Z 30 July), an upper-level ridge slowly moved across the CONUS, settling over Texas and the northern Rockies. This set the stage for the northward transport and maintenance of subtropical moisture into Colorado, creating ideal conditions for showers and thunderstorms. At 0224 MDT (0824Z), the NWS issued a Day 1 Excessive Rainfall Guidance, indicating a slight risk (10-20%) of rainfall exceeding flash flood

guidance for the western third of Colorado. Additionally, the western half of Colorado was under a marginal risk (5-10%). The initial slight risk area was limited to a small portion in the western half of our domain. By 08 MDT (14Z), rising temperatures during the early morning increased instability near the foothills of the Rockies. This, combined with a large depth of moisture to the northeast and an incoming cold front, increased the possibility of flash flooding. With surface temperatures expected to reach 80-85°F in the foothills, along with an accompanied 500-1000 J/kg of surface-based Convective Available Potential Energy (CAPE), conditions were favorable for the sustained longevity of thunderstorms. As updates from NOAA became available, the coverage area for both slight and marginal risks progressively expanded eastward, encompassing an increased portion of Colorado. At 0959 MDT (1559Z), the NWS issued updated guidance indicating that the slight risk of excessive rainfall now encompassed half of our domain, while the marginal risk extended across the western two-thirds.

At 12 MDT, a cold front initiated its southeastward movement through the northwestern region of our domain, resulting in a temperature drop in its wake and an upsurge in low level humidity preceding its arrival. The front also triggered lift near the foothills where boundary instability existed, leading to the initiation of convection. Around this time, all the necessary ingredients for localized heavy rainfall and flash flooding were present. These included slow storm motions attributable to the lack of steering winds, intensified low level convergence stemming from the outflow of convective cells, and an escalation of moisture in the low- to midlevels. Figure 3.1a shows the reflectivity later in the afternoon at 16 MDT (22Z).

Heavy rainfall was observed in the foothills of the Cameron Peak Fire (CPF) burn area, located in the northwestern part of our domain. The CPF burn area experienced significant fire activity the year prior, from August 2020 to December 2020. Throughout the evening, the threat of heavy rainfall persisted, particularly in the burn areas, which are known to increase the risk of flash flooding (Cannon et al., 2008; Merwade et al., 2008; Fox et al., 2016). By 21 MDT (03Z 31 July), precipitation became more widespread (Figure 3.1b), and the risk of flooding was further amplified by the detection of an MCV by high-resolution models, like the HRRR. As the storm progressed, radar reflectivity (Figure 3.1c) revealed the emergence of a strong cyclonic circulation within the stratiform precipitation region, indicating the presence of the MCV. Recognizing the imminent danger, a Flash Flood Warning was issued for the CPF burn area in Larimer County, which lasted for one hour.



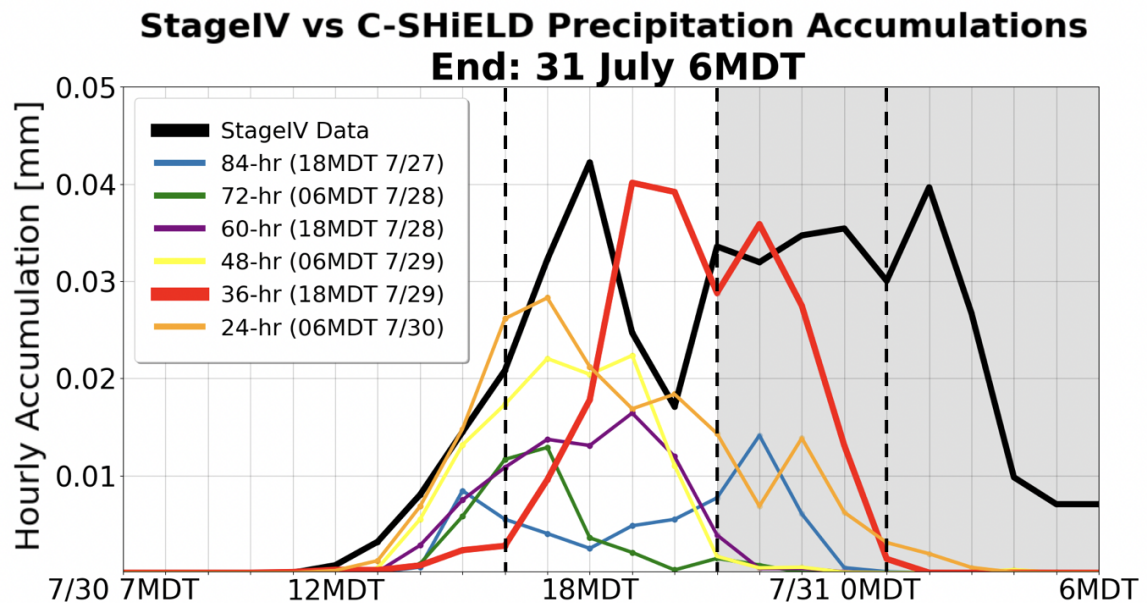
**Figure 3.1.** (a-c) Composite MRMS reflectivity (in dBZ) at 16 MDT 30 July, 21 MDT 30 July, and 01 MDT 31 July. These three specific time points represented by the MRMS reflectivity will remain consistent throughout this case study. The red rectangle is the same as a red rectangle from the previous figure. (d) 1-Day rain accumulation (mm) from StageIV observations between 6 MDT 30 July and 6 MDT 31 July.

Figure 3.1d displays the 1-day precipitation accumulation ended at 06 MDT 31 July. Precipitation patterns highlight the movement of the MCS, which was eventually directed towards the northeast. In the northwest portion of the circular domain, the CPF burn areas received 70-80 mm (2.7-3.1 in) of rain, demonstrating the substantial impact of intense rainfall in the region.

### 3.2 C-SHiELD simulation selection

The following section delves into an overview of the C-SHiELD and the reasons behind why we chose the 29 July 18 MDT forecast for further analysis.

The C-SHiELD model, distinguished by its unique approach to model gridding and parameterizations, represents a relatively new system compared to previous global models. In our assessment of the model’s performance, we analyzed six C-SHiELD forecasts and identified the most accurate simulation that closely matched observations. These forecasts, occurring every 12 hours between 27 July 18 MDT and 30 July 06 MDT (60-84 hr to 0-24 hr forecasts), provided a comprehensive evaluation of the model’s capabilities. Among them, we selected the 29 July 18 MDT run based on its superior alignment with the MRMS and StageIV datasets, along with its ability to effectively capture the storm’s characteristics, that will be explained below.



**Figure 3.2.** Hourly precipitation accumulations from the six C-SHiELD model forecasts (initialization times and forecast lead times in legend) and StageIV observations. Thick red line represents the selected C-SHiELD 36-hour forecast. The grey background after 21 MDT corresponds to nighttime in late July. The black vertical dashed lines are at 16, 21, and 01 MDT.

Figure 3.2 shows the hourly precipitation amounts for the C-SHiELD forecasts and the StageIV data aggregated within the circular domain shown in Figures 2.2b and 3.1d. Despite variations in lead time, most simulations accurately captured the onset time of

precipitation. However, the 36-hour forecast was the exception, exhibiting a 2-5 hour delay of precipitation onset. The 24-hour forecast showcased the most accurate trend in the onset of precipitation, yet the intensity was not sustained. As a whole, simulations with the longer lead times (84, 72, 60 hr) tended to underestimate precipitation rates when compared to the StageIV data. On the other hand, simulations initialized closer to the event (48, 36, 24 hr) exhibited better agreement with the observed data. Although the 36-hour simulation showed a delayed onset, it exhibited the closest match to observed precipitation rates. It is important to note that none of the simulations successfully replicated the duration of the late-night precipitation between 01 MDT to 06 MDT on the 31st, indicating premature dissipation of convection by the C-SHiELD model for this event. Given this result, our subsequent examinations focus on the 36-hour forecast.

The C-SHiELD model demonstrated a notable similarity in the 36-hour precipitation accumulation trends compared to the StageIV observations (Fig 3.2). This resemblance provides valuable insights into the influence of lead time on the accurate forecasting of convective precipitation events during the summer season. Noteworthy enhancements in the C-SHiELD model's numerical diffusion and microphysics schemes have significantly improved its predictive capabilities concerning storm location, structure, and evolution, leading to reduced model biases and enhanced diurnal cycle simulations (Harris et al., 2020). The C-SHiELD model demonstrated its ability to accurately capture the diurnal cycle for this event through all six simulations, including a simulation of a less intense event occurring one day prior (not shown). Recent investigations into C-SHiELD's averaged precipitation biases from April to August 2021 suggest a reduction in negative biases around the Colorado Front Range when compared to the months of April and May alone, indicating the potential existence of seasonal variability in precipitation biases (Kaltenbaugh et al., 2022). For this event, all C-SHiELD forecasts either underestimated precipitation accumulation trends or simulated them occurring over shorter durations than observed. These findings align with the conclusions of the aforementioned study, providing further support and validation. Kaltenbaugh et al. (2022) also found a pronounced dry bias in Colorado during the afternoon for C-SHiELD 2021. Furthermore, C-SHiELD 2021 exhibited higher sensible heat flux and lower latent heat/moisture flux compared to C-SHiELD 2020. These differences in heat fluxes are thought to be related to changes in the land surface model, which will be addressed in future research at GFDL.

Figures 3.3a-c illustrate the plan view reflectivity of the C-SHiELD 36-hour simulation at the same select times seen in Fig. 3.2. Consistent with Fig. 3.2, the growth and decay

of the C-SHiELD precipitation are evident in the plan views of the domain. At 16 MDT, convection has initiated and is beginning to intensify, supporting the low precipitation rate at this time. By 21 MDT, additional convective cells have formed, leading to an increased precipitation rate that closely resembles StageIV observations. At the final time, the system shows minimal convective activity, suggesting its premature dissipation, which is consistent with the observed low precipitation accumulation.

The MRMS Hovmöller diagram depicts meridional mean reflectivity (3.4a). It is constructed by aggregating the north-to-south values at each time across the entire domain. The multi-cellular MCS propagates from west-to-east, exhibiting enhanced reflectivity between 90-165 km. Convection initiated around 12 MDT on 30 July and persisted into the night, gradually weakening after 02 MDT 31 July. Despite a diminishing trend in reflectivity values, the storm did not completely dissipate. The C-SHiELD reflectivity Hovmöller shows that the 36-hour forecast closely matched the patterns depicted in the MRMS (Fig. 3.4b). Convection initiated in the western half of the domain around the same time, but notable precipitation occurred several hours later. The diagram showed west-to-east propagation and areas of enhanced reflectivity also between 90-160 km. Although the 36-hour forecast indicated premature dissipation of the system, it provided the most accurate representation of its longevity.

### **3.3 PSU WRF-EnKF ensemble grouping**

The following section delves into an overview of the PSU WRF-EnKF model and how we classified the 20 ensemble members into one of three groups: ‘similar to observations’ (or ‘similar to obs’ in short), ‘backheavy’, and ‘simulated MCV’.

The PSU WRF-EnKF is an ensemble-based data assimilation and forecasting system that uses the WRF model as its numerical weather prediction component. We separated the 20 ensemble members into three groups to help identify key features that contributed to their simulated evolution and respective forecast performances.

After categorizing a subset of four ensemble members as the ‘simulated MCV’ group (described later in this section), we applied the k-means clustering algorithm (from a SciPy package) to classify the remaining 16 out of 20 ensemble members into two groups based on precipitation accumulations. The groups resulting from this technique were subsequently labeled as ‘similar to obs’ and ‘backheavy’ groups. The ‘similar to obs’ group consisted of simulations that closely matched the observed precipitation evolution

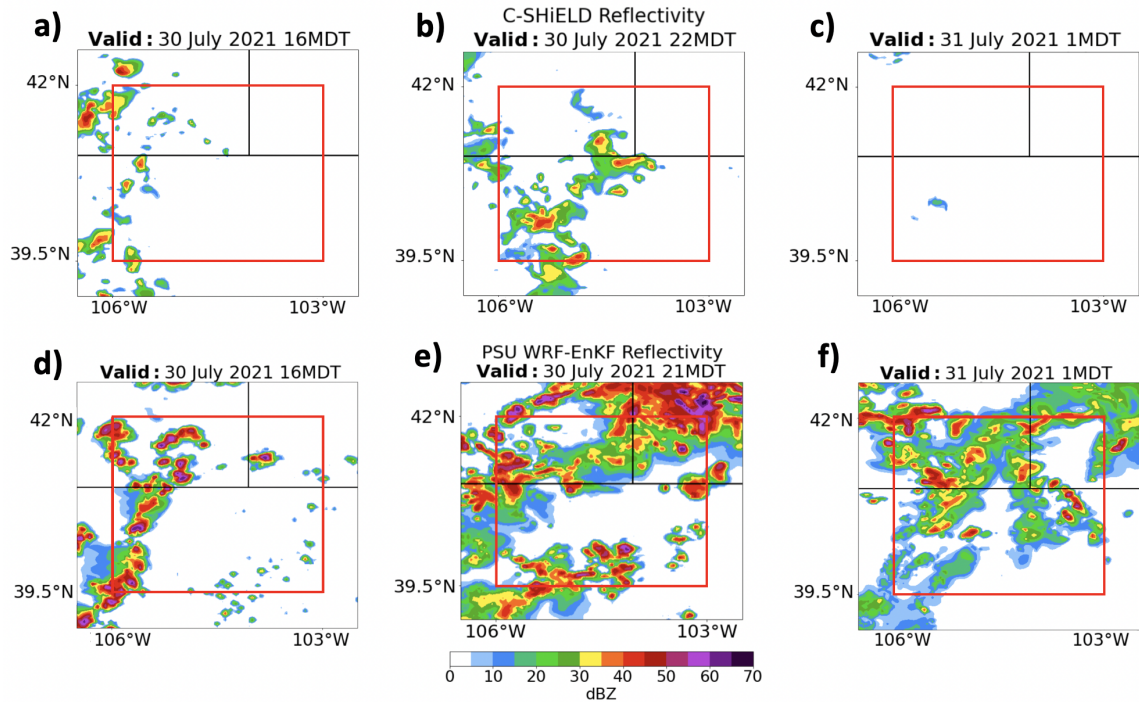


**Figure 3.3.** (a-c) Composite reflectivity plan views at 16 MDT, 21 MDT, and 01 MDT for the C-SHiELD 36-hour forecast. The red square represents our domain of interest. (d-f) Same as (a)-(c) but for PSU WRF-EnKF ensemble member #18.

from StageIV, while the ‘backheavy’ group consisted of simulations showing heavier precipitation occurring later in the lifespan of the system. Figures 3.5a-c illustrate the precipitation rates of all 20 ensemble members, as well as the StageIV observations and the selected C-SHiELD 36-hour forecast. The ensemble members are depicted by trend lines in blue, purple, or black, indicating the respective groups they belong to. The blue trend lines closely align with the StageIV precipitation trend line, indicating similar accumulation rates (Fig 3.5a). In contrast, the purple trend lines exhibit a spike in precipitation towards the end of the system’s lifecycle (Fig 3.5b).

Figures 3.3d-f illustrate the plan view reflectivity for ensemble member #18, selected from the ‘similar to obs’ group. Consistent with Fig. 3.5a, the growth and decay of this member’s precipitation are evident in the plan view of the domain. At 16 MDT, convection has just started to initiate, supporting the low precipitation rate at this time. At 21 MDT, reflectivity plan views display further convective cell initiation, and precipitation rates closely resemble those of StageIV and C-SHiELD trends (Fig. 3.5a). The WRF model exhibits a broader coverage of precipitation in the plan view compared to the C-SHiELD

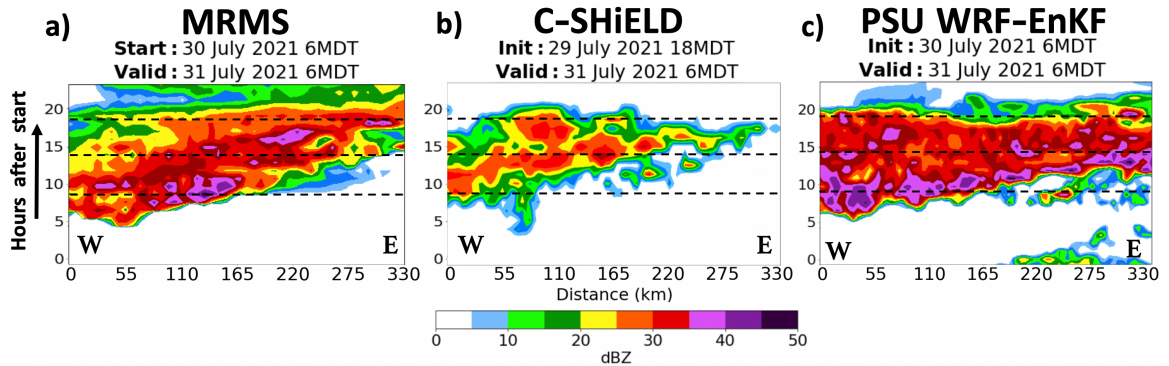


**Figure 3.4.** Hovmöller diagrams of 2-km average reflectivity (dBZ) for the (a) MRMS, (b) C-SHiELD 36-hour forecast, and (c) PSU WRF-EnKF ensemble #18. Reflectivity is averaged over the  $y$  dimension and shown as a function of  $x$  distance and time. The average is taken from the square rectangular domain from FIG 3.3. Black dashed lines denote 16 MDT, 21 MDT, and 01 MDT.

model. However, when focusing on the specific area of interest, the precipitation rates captured by both models align. The final time depicts weaker, yet sustained convective activity aligning with the precipitation accumulation trend. The associated Hovmöller diagram (Fig. 3.4c) exhibited west-to-east propagation and multiple areas of enhanced reflectivity across the 330 km domain. Convection initiated in the western portion of the domain and gradually weakened after hour 20 (02 MDT 31 July). These patterns closely aligned with those displayed in MRMS except for the absence of simulated precipitation from hours 22-24 (04-06 MDT on 31 July) (Fig. 3.4c).

Prior to our k-means clustering, we examined individual ensemble members to assess their representation of storm rotation compared to that seen in the real storm. To do this, we examined reflectivity and 500 hPa baroclinic potential vorticity (PV) plan views for each ensemble. Baroclinic PV was calculated using a Metpy package. We carefully inspected each time for rotation, focusing on the emergence of an MCV towards the end of our event. Four ensemble members were identified as having a confirmed MCV presence and constitute the ‘simulated MCV’ group. Figure 3.6 shows the plan view composite reflectivity for each of these ensemble members, along with cross sections through their estimated centers of rotation at times of their peak rotation. Each member exhibits PV anomalies above 3 km and downwind-sloping isentropes between 2-4 km altitude. Air between these levels approached the PV anomaly from the west, and ascended along the downwind-sloping isentropes, consistent with the characteristics in previous studies (Haynes and McIntyre, 1987; Raymond and Jiang, 1987; Houze, 2004). We also observed

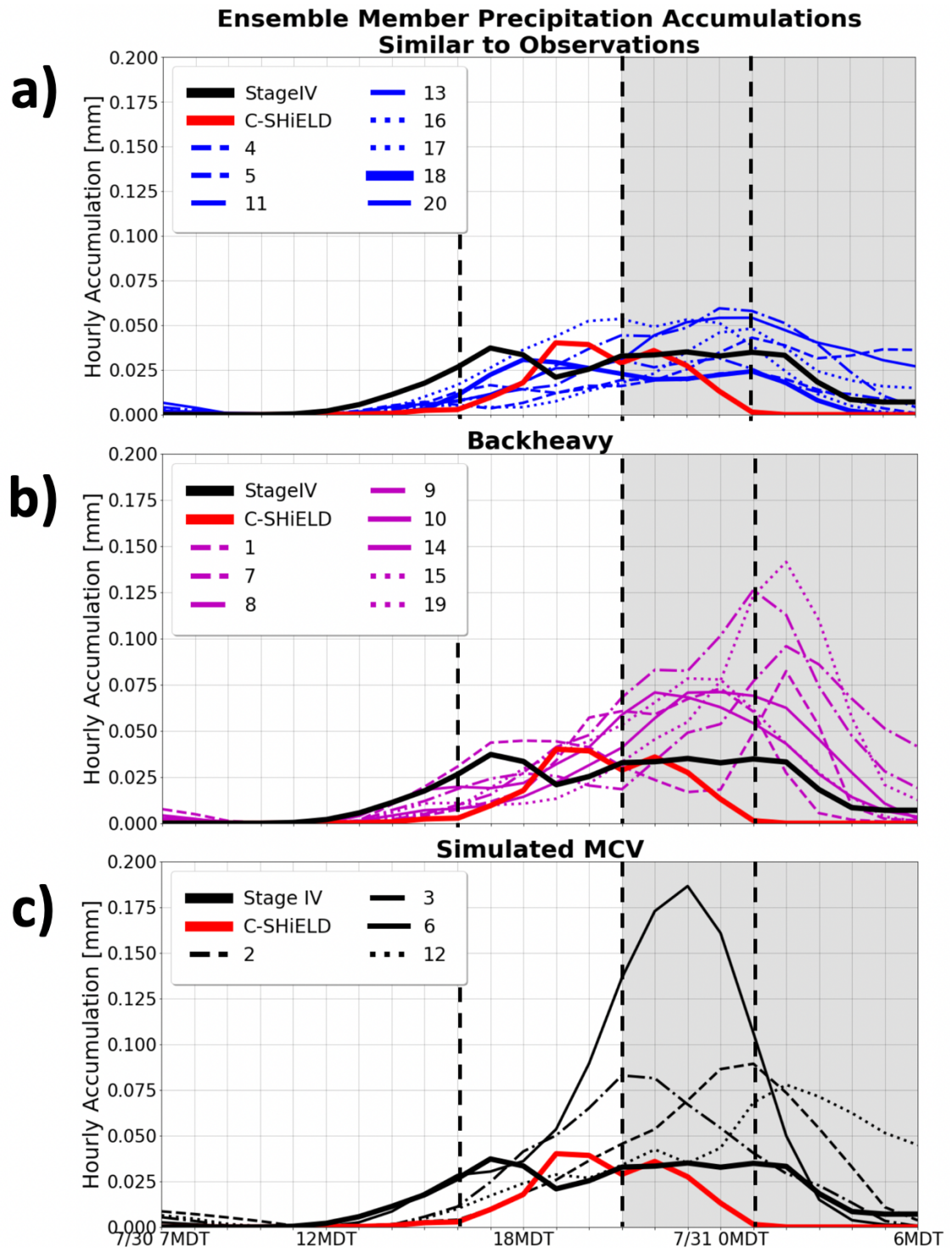


**Figure 3.5.** Hourly precipitation accumulations of the individual WRF ensemble members divided into three groups: (a) ‘Similar to obs’, (b) ‘Backheavy’ and (c) ‘Simulated MCV’ groups. The Stage IV observations and C-SHIELD 36-hr forecast accumulations are shown in black and red thick lines. The grey background corresponds to nighttime. Time points consistent from before are marked by vertical dashed lines. The color of each group indicated in the legend will remain consistent for future analyses.

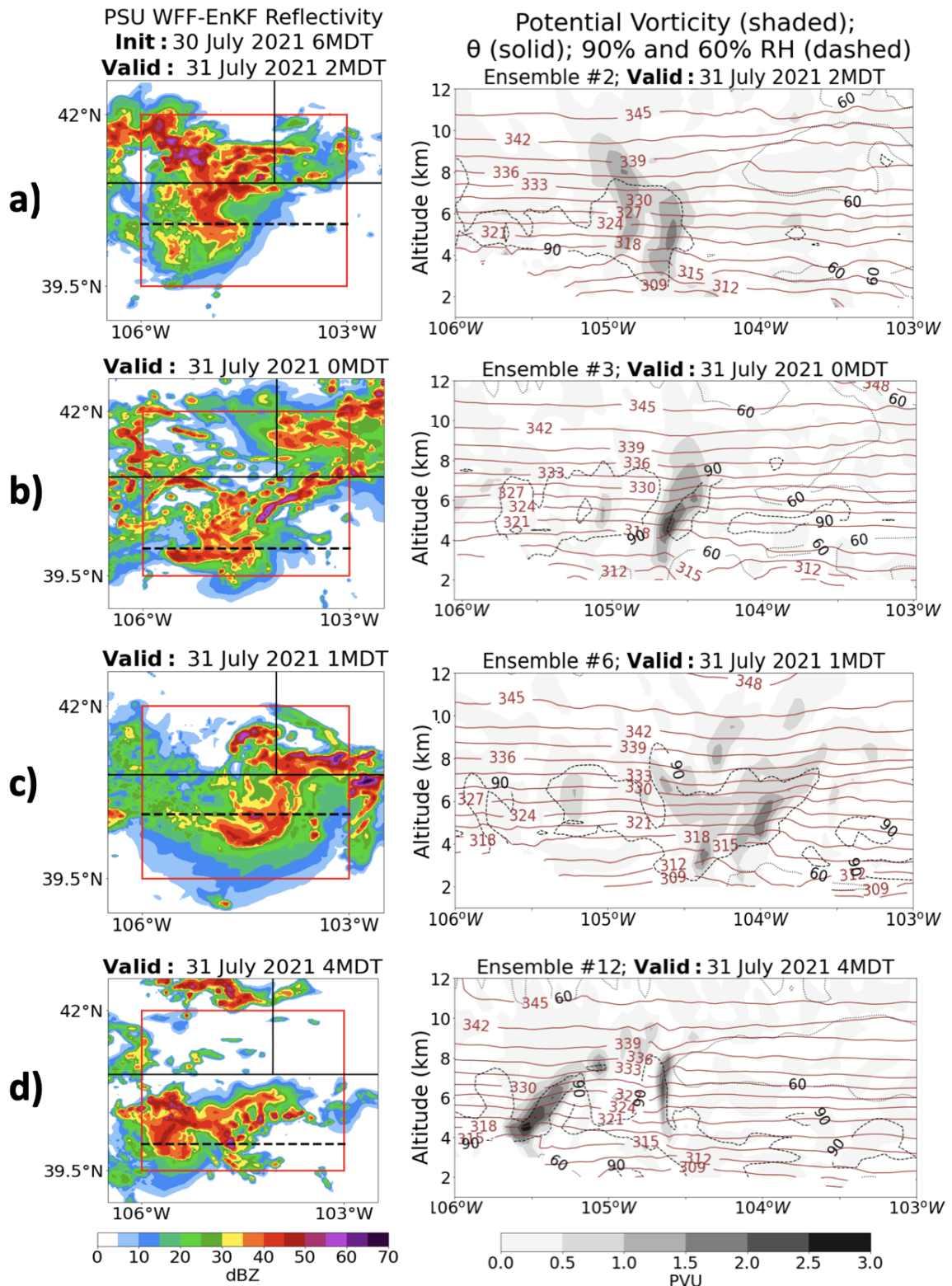


**Figure 3.6.** Left-hand column: Composite plan views of reflectivity from the 4 ensemble members of the ‘simulated MCV’ group at select times. Dashed lines indicate the locations of west-east vertical cross-sections for each ensemble member. Right-hand column: Vertical cross sections depicting: PV (shaded in  $10^{-5} \text{ m}^2 \text{ s}^{-1} \text{ K}^{-1} \text{ kg}^{-1}$ ), potential temperature (theta; red contours every 3K) and relative humidity (60% and 90% dashed lines).

that the maximum PV was located at approximately 5 km in each member. The vertical structure of the PV maximum reveals a deep, mostly upright circulation, with cyclonic PV extending through a deep layer following maximum rainfall, which aligns with the findings by Schumacher and Johnson (2008, 2009). The precipitation trends of the ‘simulated MCV’ group members are shown in Figure 3.5c.

# Chapter 4

## Results

### 4.1 Thermodynamic Assessment

To gain insights into the underlying factors influencing precipitation in our model simulations, we conducted an analysis on select thermodynamic variables. These included the calculation of convective available potential energy (CAPE) and convective inhibition (CIN) using the WRF-python package. Both parameters are crucial in severe weather forecasting (Emanuel, 1994; Rasmussen and Blanchard, 1998; Craven et al., 2002; Markowski et al., 2002; Brooks et al., 2003, 2007; Doswell and Evans, 2003; Riemann-Campe et al., 2009). CAPE quantifies the total energy that an air parcel would acquire if it were lifted from the surface to the Level of Free Convection (LFC) and subsequently rose buoyantly through the atmosphere. It is calculated as the integral of the difference between the parcel's virtual temperature and the environmental temperature, providing a measure of the potential for convection and the available energy for convective processes. We calculate the maximum CAPE using the following equation:

$$\text{CAPE} = g \int_{z_{\text{MU3000m}}}^{z_{\text{LFC}}} \frac{\theta_v - \theta_{ve}}{\theta_{ve}} dz \quad (4.1)$$

where:

$g$  is the acceleration due to gravity

$z_{\text{MU3000m}}$  is the most unstable parcel in the lowest 3 km

$z_{\text{LFC}}$  is the level of free convection

$\theta_v$  is the virtual potential temperature

$\theta_{v_e}$  is the environmental virtual potential temperature

CIN quantifies the energy required for an air parcel to overcome the energy barrier below the LFC. It represents a constraining factor that can inhibit convection, even in the presence of high CAPE values (Williams and Renno, 1993; Riemann-Campe et al., 2009). Both variables are vital indicators for CI, which occurred at 12 MDT.

We generated domain-averaged time series plots for the C-SHiELD 36-hour forecast and each WRF group to examine temporal variations of CAPE, CIN, and other select variables. Average values (within the rectangular domain; see Fig 2.2b) were calculated for each ensemble member, then averaged within each group to create time series plots (Fig 4.1). For CAPE, time series revealed that both the ‘backheavy’ and ‘simulated MCV’ groups exhibited comparable values, both 2 hours prior to and after CI, with slightly higher values than both the C-SHiELD output and ‘similar to obs’ group (Fig 4.1a). At 16 MDT, the ‘simulated MCV’ group had surpassed the ‘backheavy’ group trend, with a domain-averaged CAPE value reaching approximately 660 J/kg. The other three groups reached their maximum CAPE values one hour earlier. At 21 MDT, both the ‘backheavy’ and C-SHiELD group trends exhibited a sudden increase in CAPE, although this rise was short-lived in the C-SHiELD. By 23 MDT, the ‘backheavy’ group reached its second peak CAPE value of approximately 550 J/kg. Maxima in convective precipitation are typically preceded by peaks in CAPE, and both groups demonstrated this pattern (Fig 3.5b). Following this precipitation peak, CAPE values in all groups consistently declined until the storm exited the domain.

The analysis of domain-averaged CIN trends revealed that all three WRF groups exhibited relatively low CIN values in the hours preceding CI, with values ranging between 25-50 J/kg (Fig 4.1b). As we get closer to CI, the CIN values for all WRF groups progressively decrease, eventually reaching values close to 0 J/kg. Interestingly, the C-SHiELD exhibited higher CIN values in the hours leading up to CI compared to the WRF groups. The C-SHiELD eventually aligned with the WRF trends, approaching values near 0 J/kg. However, C-SHiELD exhibited a prolonged delay of two hours compared to the WRF groups in reaching this threshold. Domain-averaged CIN values remained low until 16 MDT for all groups. At this time, the C-SHiELD simulated a faster increase in CIN. The higher initial CIN values in the C-SHiELD indicated that the lower-levels were initially more stable and CI was more difficult to achieve. This may explain why C-SHiELD precipitation occurred generally later than most WRF ensemble

members (Figures 3.5a-c). Afterwards, the fast increase in CIN can be explained by the redevelopment of a low level stable layer during the later stages of the convective event (Barkidija and Fuchs, 2013).

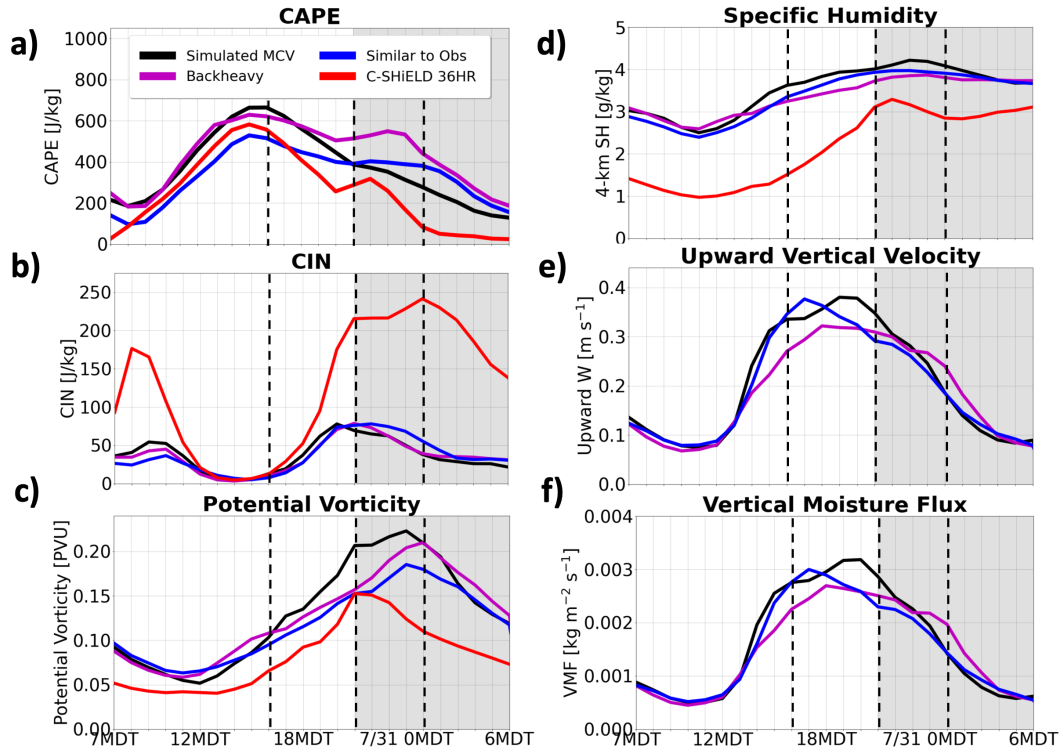


**Figure 4.1.** Time series depicting the evolution of (a) CAPE, (b) CIN, (c) 500 hPa PV, (d) 4 km specific humidity, (e) 4 km vertical velocity, and (f) 4 km vertical moisture flux (VMF) within the square domain of interest for C-SHIELD and each averaged WRF group. Analysis time points still indicated by dashed vertical lines, and the grey background corresponds to nighttime.

The average CAPE and CIN shown does not fully describe the distribution of these values within the individual WRF ensemble members. Therefore, histogram analyses were conducted for each ensemble member with time to ensure that the domain-averaged CAPE and CIN time series were representative of the domain. Figure 4.2 shows a normalized frequency count of nonzero CAPE and CIN values within each model group. Calculations are made at each domain grid point, counted over all individual simulations within each group, and normalized by the number of grid points within each bin by the total number of grid points in each group.

At 16 MDT, the histogram revealed the ‘simulated MCV’ group with the highest percentage of CAPE pixels between 1001-2500 J/kg. This is followed closely behind by the ‘backheavy’ group. In contrast, both the ‘similar to obs’ and C-SHIELD groups had

more grid points between 1-500 J/kg. The C-SHiELD group also manifests the greatest percentage in CIN between 1-75 J/kg. At 21 MDT, the C-SHiELD showed the highest number of CAPE pixels between 1-500 J/kg, while the ‘backheavy’ group displays more between 501-2000 J/kg. As for CIN, the C-SHiELD had the greatest number of grid points between 225-450 J/kg. At 1 MDT, the C-SHiELD simulation once again exhibited the greatest frequency CAPE pixels between 1-500 J/kg, along with the highest frequency of CIN between 151-450 J/kg. The relative evolutions of the distributions corroborate the group average trend lines seen in Figures 4.1a and 4.1b. Greater frequency of lower CAPE pixels is consistent with the lower domain-averaged CAPE. This was clearly shown at most times in the C-SHiELD. Moreover, higher frequency of greater CAPE pixels in the WRF groups corresponded to higher domain-averaged CAPE.

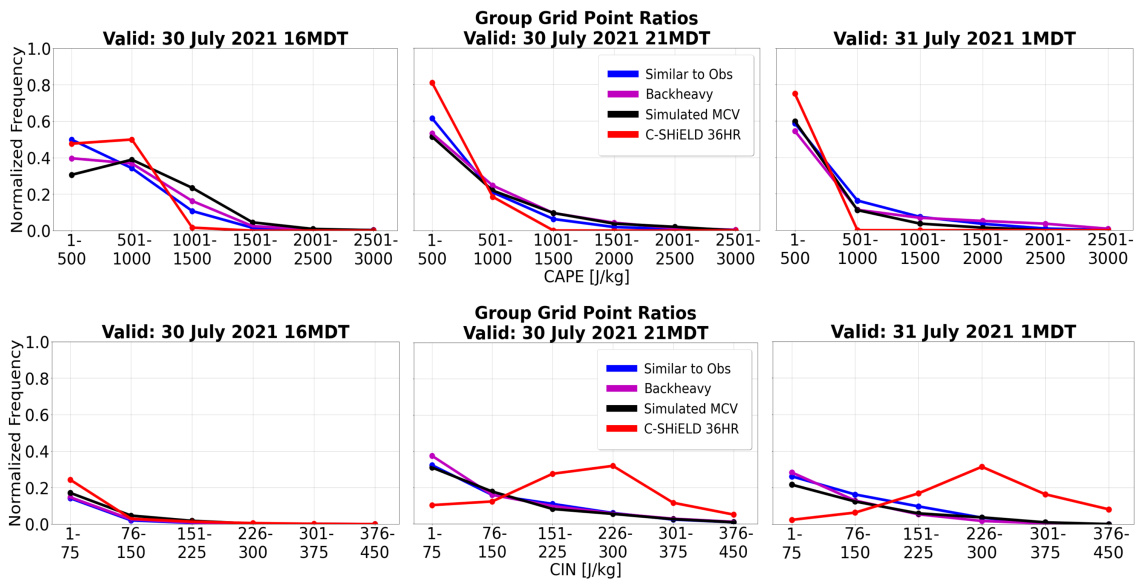


**Figure 4.2.** Histograms of CAPE (top row) and CIN (bottom row) domain averages from each model group. Evaluation times align with the previous time selections. Frequencies are normalized by the number of grid points within the domain.

Figure 4.1c presents the time series of domain-averaged 500 hPa PV. The C-SHiELD group consistently displayed the lowest PV values compared to the WRF groups. From 17 MDT 30 July to 01 MDT 31 July, the ‘simulated MCV’ group consistently exhibits the highest PV values. This is expected due to the elevated PV cores that define an MCV (Houze, 2004). Notably, ensemble #6 recorded the highest precipitation rate amongst all ensemble members, while also simulating an MCV. The development of MCVs in these members is attributed to their elevated CAPE and the presence of broad

stratiform precipitation during the later stages of the convective life cycle. Rotation became important between 20-04 MDT 30-31 July across all ensembles in this group. As the storm progressed through time, the contribution of stratiform precipitation, which has been recognized as a significant source of midlevel PV generation (Raymond and Jiang, 1987; Conzemius and Montgomery, 2009), became increasingly prominent.

Figure 4.1d shows the specific humidity time series at 4 km altitude for each group. We are looking at midlevel specific humidity to examine how much dry-air entrainment plays a role in inhibiting convection. WRF group trends follow similar patterns at all times, while the C-SHiELD displays consistently lower values. Midlevel moisture is advected into the domain in the hours succeeding CI, and the C-SHiELD simulation reaches moisture values closer to those seen with the WRF, however, values are still lower on average. Integrated moisture content was also computed to assess the potential for dry-air entrainment and the availability of a moisture source for convection. Results show the ‘similar to obs’ group consistently displayed 1 g/kg less moisture than the other WRF groups until 01 MDT 31 July. The C-SHiELD still exhibited much less moisture in the atmosphere than the WRF groups (not shown). Given the departure of the C-SHiELD data from similar fields in the observation and WRF datasets, any additional claims will require further investigation. Moreover, we were working with limited vertical levels in the C-SHiELD. As such, the rest of the study will focus on the WRF output.

Figures 4.1e and 4.1f depict the time series of domain-averaged vertical velocity and vertical moisture flux, as these variables are directly related to precipitation generation. Both variables display similar trends, with peaks in vertical velocity aligning with peaks in vertical moisture flux. Vertical moisture flux is the result of multiplying specific humidity by vertical velocity, which explains variations observed amongst the trend lines. At 17 MDT, the ‘similar to obs’ and ‘simulated MCV’ groups exhibit the highest values for both vertical velocity and VMF. At 21 MDT, the ‘simulated MCV’ line displays maximum values for these variables whereas at 01 MDT, the ‘backheavy’ group demonstrates comparable peaks.

## 4.2 Representative Group Soundings

In this section, we analyze representative ensemble member soundings from the three WRF groups to observations to study the vertical structure of their thermodynamic environment. First, we generated domain-average soundings for each group using the area

of a small square within our domain on interest, with dimensions approximately from 105°W to 104.5°W and 40°N to 40.5°N. This selection was due to its strategic position before CI and enabling observations of the environment during storm intensification and dissipation. We then plotted the average sounding of each group across select times to identify key differences in atmospheric characteristics and identified the ensemble member that had the sounding that best matched the group average. Figure 4.3a displays one CSU-launched sounding from the "PRE"-CIP campaign, and Figure 4.3b-c are soundings from NWS Denver. Figure 4.4 shows the evolution of the vertical profile within our domain over the course of 30 and 31 July 2021 at 16 MDT, 21 MDT, and 01 MDT for each WRF group (rows a, b and c). Soundings and their respective statistics were calculated using a Metpy package.

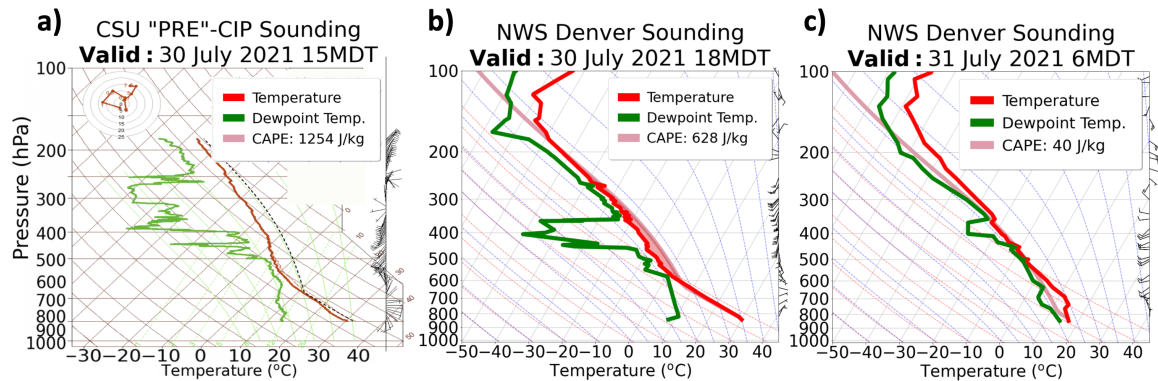


**Figure 4.3.** Observational soundings from (a) CSU Radiosonde and (b-c) NWS Denver at select times during the event.

The CSU-sounding data shows a consistent dewpoint temperature difference of  $\sim 10^{\circ}\text{C}$  below the 500 hPa temperatures. As we ascend to 400 hPa, this difference increases to  $\sim 30^{\circ}\text{C}$ . The sounding was released about one hour prior to each group's maximum CAPE. At 18 MDT, the NWS Denver sounding exhibited a distinct dry-pocket of air within the 350-500 hPa range, alongside notably high CAPE values. By 6 MDT the next day, a smaller dry layer was still present along with a considerable reduction in atmospheric instability.

At 16 MDT, the 'similar to obs' group exhibited dewpoint temperatures in the 300-500 hPa layer that were  $\sim 20^{\circ}\text{C}$  below the temperature. Despite having a relatively large CAPE value, this presence of a midlevel dry pocket likely allowed for dry air entrainment that limited precipitation production. At 21 MDT 30 July, drier midlevels remained present, consistent with observations. But by the end time 01 MDT 31 July, the profile was

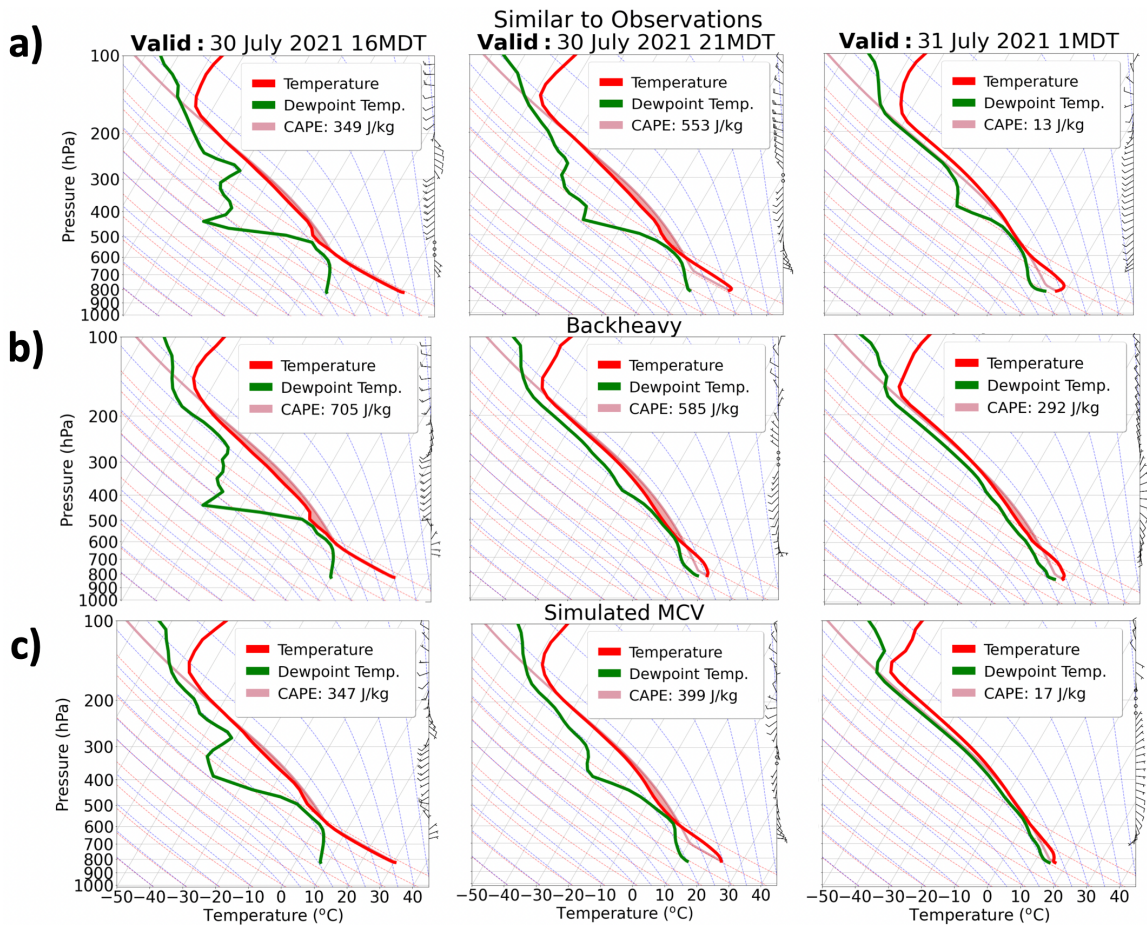


**Figure 4.4.** Soundings shown for one representative ensemble member in each group at 16 MDT, 21 MDT, and 01 MDT. Row (a) shows an ensemble member #4 from the ‘similar to obs’, (b) is #15 from the ‘backheavy’ group, and (c) is #3 from the ‘simulated MCV’ group.

near the saturated moist adiabat with moister midlevels, and little CAPE indicating a diminished likelihood of future convection. We expect that longer-lasting and heavily precipitating convection tends to have some notable low level wind shear that organizes the convection to have mesoscale downdrafts that help build and sustain the updrafts feeding the system (Zipser, 1977; Rotunno and Klemp, 1982; Rotunno et al., 1988; Fovell and Ogura, 1989; Sherburn and Parker, 2014; Chen et al., 2015; Marion and Trapp, 2018; Gray and Frame, 2019). In this case at all three times, the low levels (below 600 hPa) exhibited weak surface winds and weak wind shear (5-15 kt), which is consistent with this group having the lowest precipitation total of the three groups.

The ‘backheavy’ ensemble has similar characteristics to the ‘similar to obs’ group at 16 MDT, including low level easterlies and no notable low level shear. The midlevels were

dry just as in ‘similar to obs’, indicating a higher potential for midlevel drying through entrainment (Morton et al., 1956; Scorer, 1957; Morrison, 2017; Morrison et al., 2020a; Peters et al., 2020; Mulholland et al., 2021). By 21 MDT, the group shows increased low level wind shear and surface winds, supporting differences in precipitation evolutions when compared to ‘similar to obs’. Moist midlevels and high CAPE values also created a favorable environment for sustained convection. The contrasting midlevel moisture between the ‘backheavy’ and ‘similar to obs’ groups may be attributed to distinct initial conditions. At 01 MDT, the group exhibits low level southerly winds and wind shear, with relatively higher CAPE values suggesting the potential for sustained convective development. These variations provide insights into the group’s late night maximum precipitation.

The ‘simulated MCV’ group at 16 MDT had a profile that was slightly more moist than the other groups indicating a more favorable thermodynamic environment for sustained convection. By 21 MDT, this group showed relatively moist midlevels, suggesting a better environment for convection compared to the ‘similar to obs’ group. Low level shear is similar to that of the ‘backheavy’ group. CAPE and moisture for the ‘simulated MCV’ group are lower than the ‘backheavy’ group, which supports the domain-average CAPE values, but differs slightly from precipitation analyses. At 01 MDT, we see an environment with weak midlevel shear and stronger low level shear, which are typically observed in MCV environments (Bartels and Maddox, 1991). The low CAPE indicates the storm has started to dissipate.

### **4.3 Reflectivity CFADs**

So far we have examined the simulated horizontal precipitation structures in plan views and in Hovmöller diagrams. In this section, we explore the vertical structure of reflectivity by using Contoured Frequency by Altitude Diagrams (CFADs; Yuter and Houze, 1995; Masunaga et al., 2008; Satoh et al., 2010; Huang et al., 2015; Friedrich et al., 2016; Chen et al., 2016). They are constructed by binning data at each altitude and calculating the frequency of occurrences. This results in relative occurrences of the variable at different altitudes. With CFADs, we can uncover new patterns and changes in reflectivity distributions across each WRF group. CFADs provided valuable insights into the characteristics and patterns throughout the convective systems’ life cycle, uncovering variations in their dynamics and thermodynamics. By comparing CFADs of reflectivity

between the WRF groups, specific attributes and differences in their vertical structures can be discerned, thus enhancing our understanding of the unique features and behaviors exhibited by each convective group.

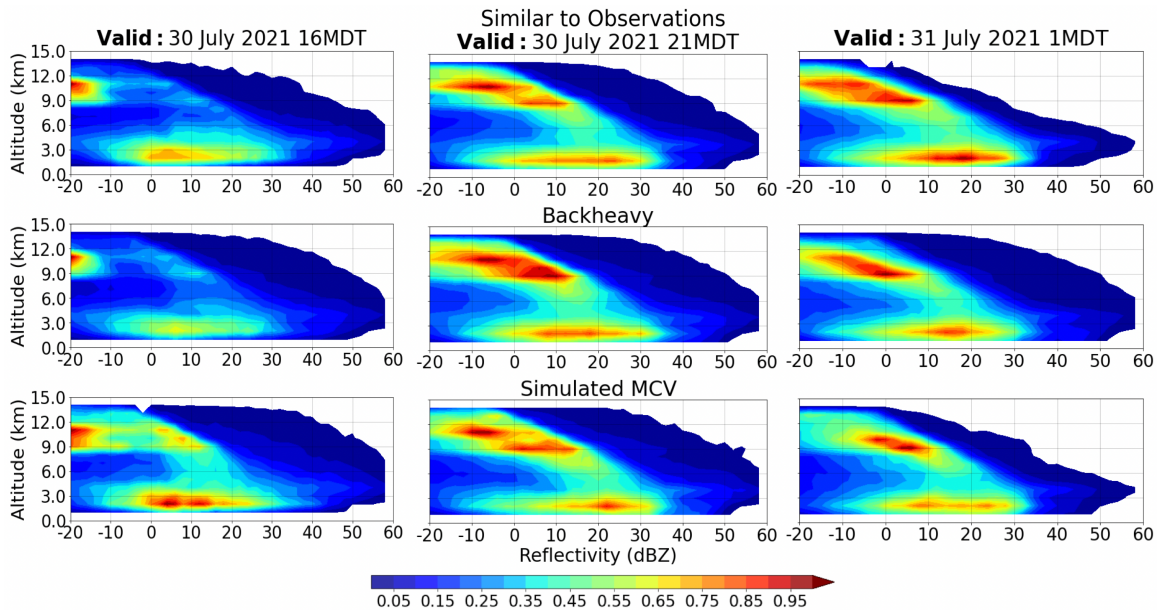


**Figure 4.5.** Reflectivity CFADs for each WRF group at 16 MDT (left), 21 MDT (middle) and 01 MDT (right). Reflectivity CFADs were binned every 2 dB and normalized by the maximum frequency at each time.

Figure 4.5 shows the reflectivity CFADs for the three WRF groups, providing consistent representations of the chosen time intervals. Negative reflectivity values are indicative of smaller particles, including raindrops and ice, that contribute to the overall reflectivity measurements. Difference plots in Figure 4.6 offer valuable insights into the contrasting features and variations between the ‘backheavy’ and ‘simulated MCV’ groups compared to the ‘similar to obs’ group, visually depicting deviations in reflectivity frequencies at each vertical level. At 16 MDT, the ‘simulated MCV’ group shows a greater frequency of strong reflectivity values (20-45 dBZ) in the lower atmosphere between 1-3 km altitude compared to the other two groups. Additionally, reflectivity values exceeding 40 dBZ are more prevalent at higher altitudes, particularly between 4-7 km, indicating the strength of the reflectivity cells likely due to stronger updrafts. These features can be most clearly seen in the positive values of the ‘simulated MCV’ difference plot. Moreover, the MCV group displays a peak of -20-20 dBZ occurrences between 9-12 km, indicating the presence of ice in the upper-levels (Fig 4.5). The ‘simulated MCV’ group exhibits

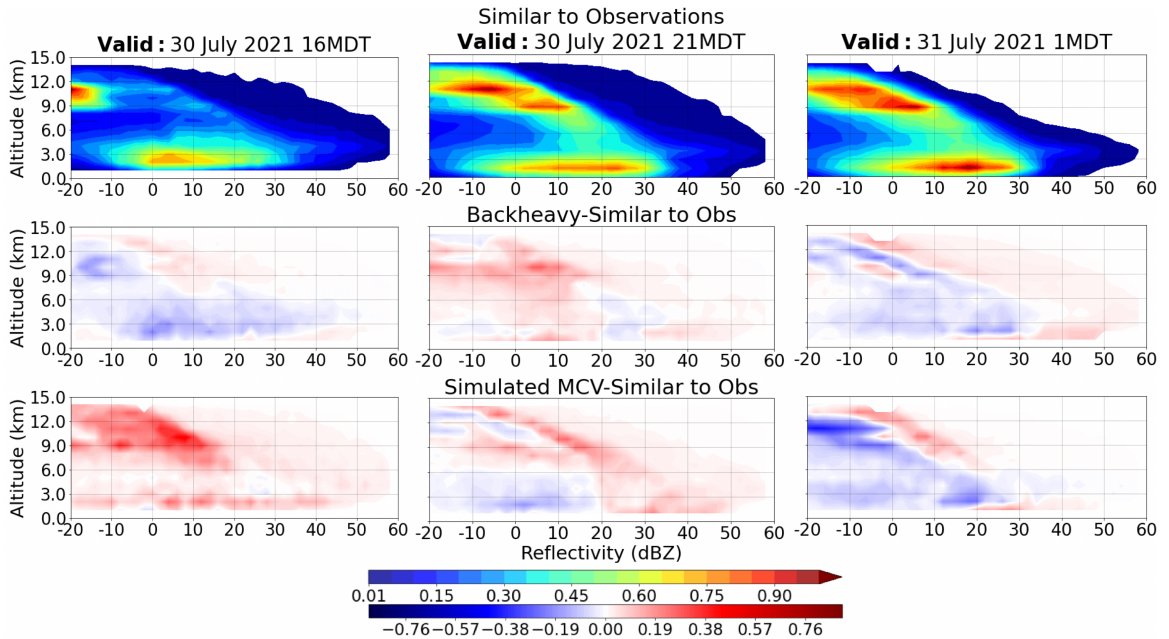


**Figure 4.6.** Top row shows the same CFADs from ‘similar to obs’ group in Fig. 4.5. Second and third rows show reflectivity CFAD difference plots at the same times. Red colors represent higher frequencies compared to the ‘similar to obs’ group, and blue colors portray lower frequencies than the ‘similar to obs’ group.

distinct evidence of strong convective precipitation. The ‘backheavy’ group has a higher frequency of 0-30 dBZ occurrences between 7-12 km values compared to the ‘similar to obs’ group, but not as high as the ‘simulated MCV’ group. Both the ‘backheavy’ and ‘similar to obs’ groups show indications of convective precipitation, but their intensity is not as pronounced as in the ‘simulated MCV’ group. Furthermore, a wide range of reflectivity values below 2 km altitude is present in all groups, which is a clear sign of evaporation.

At 21 MDT, in the lower atmosphere (1-3 km), the ‘similar to obs’ and ‘simulated MCV’ groups peak near 25 dBZ, while the backheavy group peaks between 10-20 dBZ. But they are all becoming more stratiform in nature as the peak of reflectivity occurrences near 5 km becomes more sharpened, representative of the radar bright band (Fig 4.5). Compared to ‘similar to obs’, both the ‘backheavy’ and ‘simulated MCV’ groups exhibit larger frequencies of high reflectivities at nearly all altitudes, with the ‘simulated MCV’ having the larger positive values in the difference plots.

At 01 MDT, two distinct patterns emerge in the CFAD analysis for each group. First, ‘similar to obs’ shows the highest frequency of low reflectivity (5-30 dBZ) between 2-3

km altitude, indicating overall weaker stratiform precipitation as seen in the precipitation evolution plots. In contrast, the ‘backheavy’ group shows a heightened frequency of 35-60 dBZ through the first 12 km of the atmosphere. The ‘simulated MCV’ group also has slightly larger reflectivities, particularly above 6 km altitude. But these are not as prominent as the ‘backheavy’ group, which is consistent with the widespread greater reflectivity values and intensified precipitation rates at later times which defines this group.

#### **4.4 Vertical Velocity and Vertical Moisture Flux CFADs**

Building upon the insights provided by the reflectivity CFADs, our analysis of vertical velocity explores the distribution and behavior of updrafts within each group. These CFAD plots, depicted in Figures 4.7 and 4.8, showcase the evolution and strength of the updrafts in each group. Frequencies over 1000 grid points were excluded to highlight the lower frequency of higher vertical velocity. At 16 MDT, the ‘simulated MCV’ group exhibits more pronounced and broad updrafts of 2-15 m/s between 3-12 km altitude. We also see the ‘backheavy’ group displaying elevated updrafts of 2-12 m/s between 7-12 km. By 21 MDT, the ‘simulated MCV’ group presents the deepest and strongest updrafts of 2-13 m/s between 2-11 km altitude. The ‘backheavy’ group reveals moderately forceful updrafts of 5-13 m/s in the midlevels between 5-9 km altitude. Finally, at 01 MDT, the ‘backheavy’ group showcases the most robust values of 2-15 m/s between 2-12 km altitude, while the ‘simulated MCV’ and ‘similar to obs’ groups exhibit comparatively lower vertical velocity values. The ‘simulated MCV’ group, however, has stronger updrafts of 3-7 m/s between 4-9 km altitude when compared to ‘similar to obs’.

Observations gleaned from the reflectivity and vertical velocity CFADs aid in our examination of VMF (Figs 4.9 and 4.10), which closely relates to precipitation rates. At 16 MDT, both the ‘similar to obs’ and ‘simulated MCV’ groups exhibit greater moisture flux values ( $0.01-0.02 \text{ kg m}^{-2} \text{ s}^{-1}$ ) between 2-4 km altitude. In contrast, the ‘backheavy’ group shows the lowest frequency at these altitudes, which corresponds to its low precipitation rate. Despite the ‘similar to obs’ group having greater VMF values than the ‘backheavy’ group in the lower-levels, it exhibits the lowest frequency of occurrences between 5-8 km altitude. This discrepancy is consistent with the presence of the dry-air pocket observed in the group sounding at this time, indicating stronger entrainment and also limiting the precipitation rate in this group.

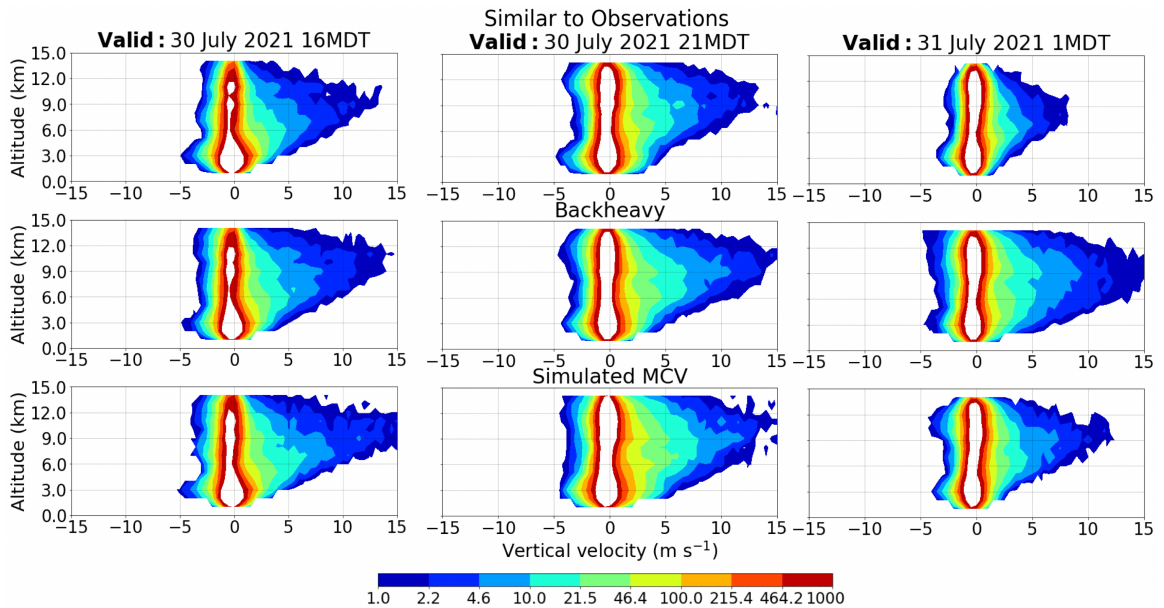


**Figure 4.7.** Vertical velocity CFADs for each WRF group at 16 MDT (left), 21 MDT (middle) and 01 MDT (right). Velocity CFADs were binned every 0.5 m/s. The Contour colorbar is on an exponential scale. Frequencies above  $10^3$  are excluded to highlight the relatively lower occurrences of higher vertical velocity values.

At 21 MDT, there is a pronounced increase in VMF across all groups. The ‘simulated MCV’ group exhibits the most obvious rise, with frequencies of  $0.02\text{-}0.07 \text{ kg m}^{-2} \text{ s}^{-1}$  displayed between 2-6 km altitude. This increase in low to midlevel moisture, coupled with strong updrafts, contributed to enhanced reflectivity signals between 9-12 km altitude and overall higher precipitation rates. Similarly, the ‘backheavy’ group showed notable increases in both vertical velocity and VMF, resulting in slightly less prominent but still noteworthy frequencies of high reflectivities at various altitudes, and an increasing precipitation rate.

At 01 MDT, both the ‘similar to obs’ and ‘simulated MCV’ groups demonstrate similar patterns in VMF, with maximum values of  $0.03\text{-}0.04 \text{ kg m}^{-2} \text{ s}^{-1}$  between 3-6 km altitude. However, the distinguishing factor between both groups lies in the strength of their updrafts. This distinction is manifested by slightly higher reflectivity values above 6 km altitude and greater precipitation rates in the ‘simulated MCV’ group. In contrast, the ‘backheavy’ group exhibited the largest increase in VMF of  $0.04\text{-}0.07 \text{ kg m}^{-2} \text{ s}^{-1}$  between 2-6 km altitude. This observation, combined with strong updrafts, supports the sustained convective activity manifested within this group.

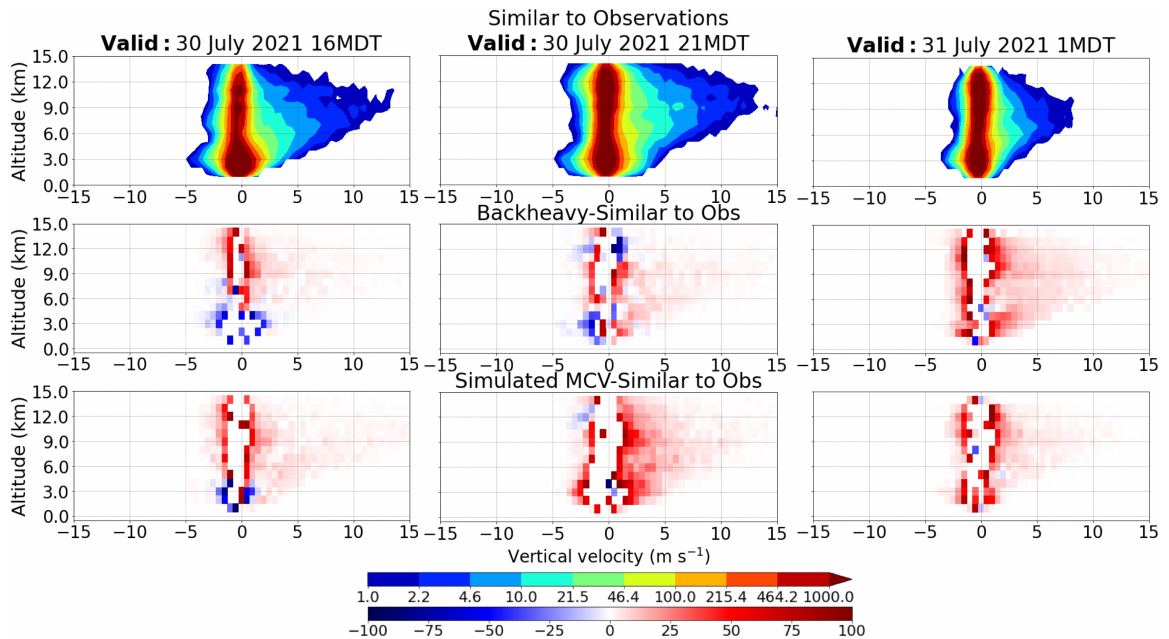


**Figure 4.8.** Top row shows the same CFADs from ‘similar to obs’ group in Fig. 4.7. Second and third rows show vertical velocity CFAD difference plots at the same times. Red colors represent higher frequencies compared to the ‘similar to obs’ group, and blue colors portray lower frequencies than the ‘similar to obs’ group.

## 4.5 Convective-to-Stratiform Life Cycle

To comprehensively analyze the convective systems’ life cycle of convective to stratiform precipitation in each group, we calculated the vertical mass transport (VMT) within each domain at our select times. The VMT shows the dominant direction of air transport, revealing prevailing patterns within each group, and detects changes in transport dynamics over time. The convective system life cycle generally consists of four stages (Houze, 1997). In the initial stage, there is dominant positive vertical mass transport in the low- to mid-levels, accompanied by strong upward motions throughout the atmosphere. Downdrafts are present but less pronounced. This stage is characterized by convective precipitation and maximized vertical mass transport in the lower levels. The second stage sees a shift in the peak of vertical mass transport to higher altitudes, with a more negative trend at the surface and increased downdrafts. The third stage is characterized by predominant stratiform precipitation. Weak updrafts above the melting level promote cloud and precipitation persistence through vapor deposition, while below the melting level, net downward transport with weaker vertical velocities occurs due to evaporation.

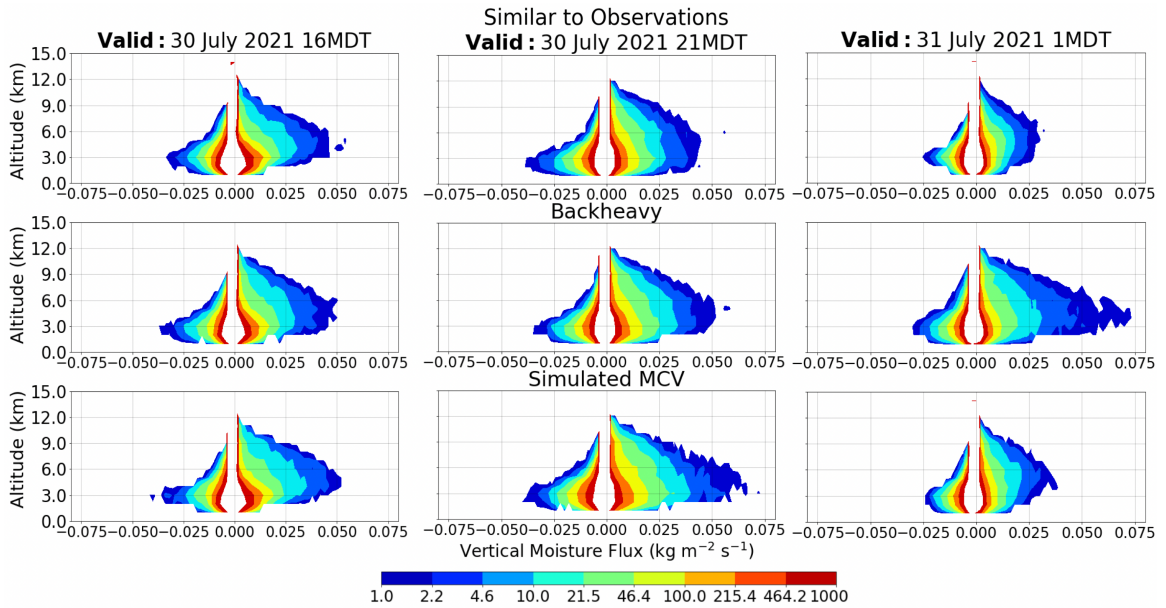


**Figure 4.9.** As in Figure 4.7, but for vertical moisture flux (VMF). VMF frequencies were binned every  $0.002 \text{ kg m}^{-2} \text{ s}^{-1}$ .

The final stage marks the weakening of the convective system over time.

The VMT is calculated by multiplying the density and vertical velocity values at each grid point across various levels. These calculated VMT profiles are then averaged over each domain grid point for each ensemble member, then they are averaged over each ensemble member to yield group average VMT profiles. Figure 4.11 shows the profiles. The positive, negative, and net VMT values were calculated separately, then normalized using the maximum positive value among the three groups with time.

Distinct patterns emerge in each group at 16 MDT, as shown in Figure 4.11. The ‘simulated MCV’ group exhibits upward net transport starting directly at the lowest altitude. In contrast, the ‘similar to obs’ and ‘backheavy’ groups exhibit upward net transport above 3 km altitude, while small downward net mass transport occurs below. The ‘simulated MCV’ group displays a bottom-heavy profile that is typical of convective precipitation with dominant low level upward mass transport, which is consistent with the early time of the diurnal convection life cycle (Houze, 2004; Didlake and Houze, 2013). The other two groups likely have significant convective precipitation as well, but it is likely that evaporative cooling is occurring in the low levels to produce the small downward mass transport. This is consistent with the drier midlevels, the wide range of reflectivity values also occurring at 2 km altitude and weaker updrafts seen in the vertical

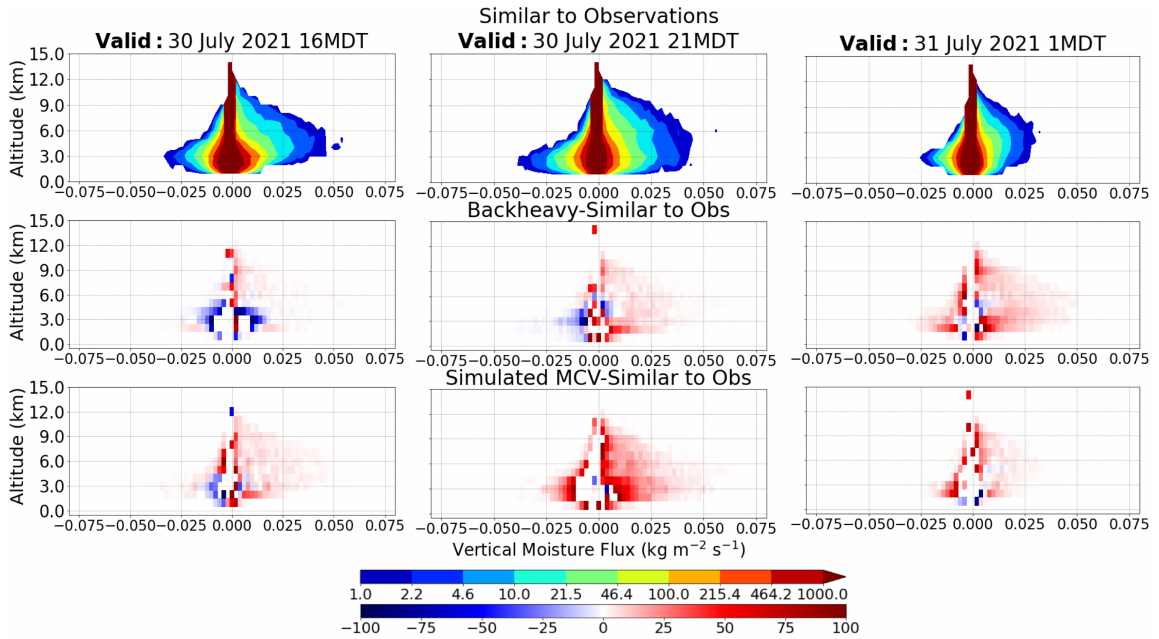


**Figure 4.10.** As in Figure 4.8, but for VMF.

velocity plots.

At 21 MDT, we observe consistent net transport patterns above 2-3 km altitude in both the ‘similar to obs’ and ‘backheavy’ groups, with a less pronounced downward net transport in the lower levels of the ‘similar to obs’ group compared to the previous time. Additionally, the ‘simulated MCV’ group exhibits even stronger upward net transport between 1-2 km altitude, reinforcing the observed pattern. Moreover, it is noteworthy that between 4-6 km, there is a slightly greater upward transport observed across all groups compared to the previous time. This corroborates the clear increase in frequency occurrences shown in the reflectivity CFADs, indicating growing convective precipitation for all three groups.

At 01 MDT, the ‘similar to obs’ group showcases weaker net vertical mass transport up to 3 km altitude, succeeded by a sudden surge in mass transport. The weaker net mass transport corresponds to the weakening precipitation in this group at this time. Conversely, the ‘simulated MCV’ and ‘backheavy’ groups manifest robust net downward transport below 4 km altitude. Notably, the ‘backheavy’ group exhibits two prominent peaks, one above and the other below 5 km altitude. This net upward transport above the melting layer and net downward transport below signifies the presence of stratiform precipitation at this later time. The other two groups show signs of weaker stratiform precipitation. The

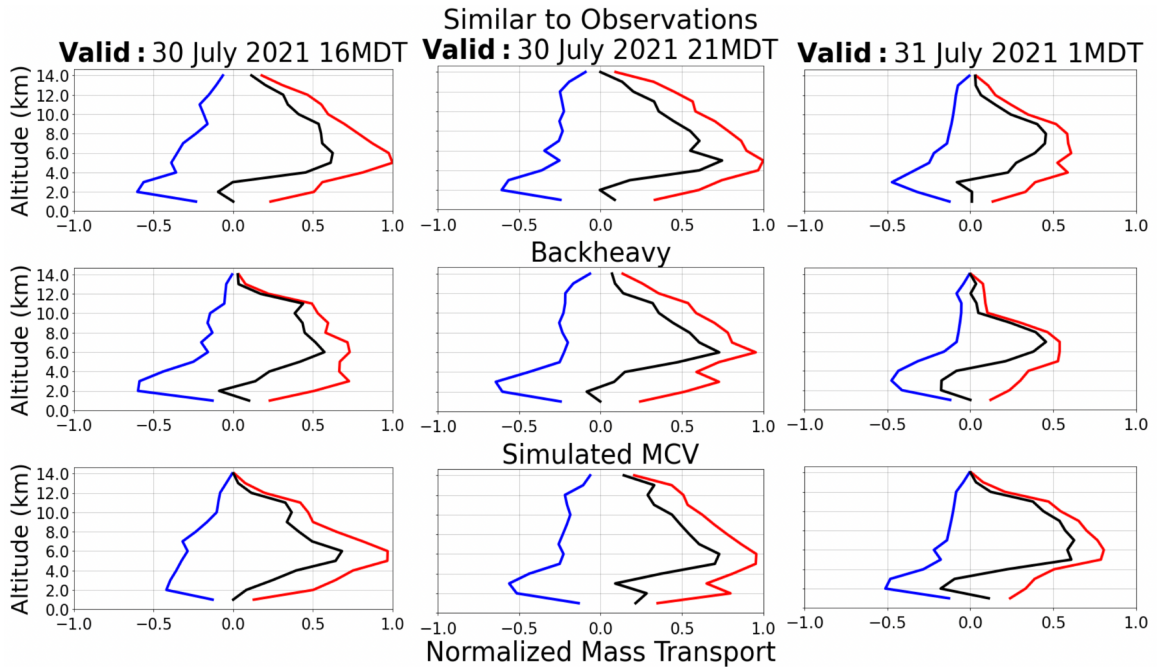


**Figure 4.11.** Vertical mass transport (VMT) profiles for each group at select times. Positive (red), Negative (blue), and Net (black) VMT profiles for each group at analysis times. VMT profiles are normalized by the maximum positive VMT.

‘simulated MCV’ group demonstrates a notable pattern of net downward mass transport in the lower levels, which corresponds to the presence of downdrafts observed in the vertical velocity CFADs. This downward mass transport is further supported by the higher frequency of VMF directed downward between 2-4 km altitude. The increased VMT between 5-10 km altitude can be attributed to the transport of smaller ice particles, indicative of previously strong updrafts. The ‘similar to obs’ group exhibited the weakest indications of stratiform precipitation, supported by the net zero VMT in the low levels. Additionally, the low frequency of VMF occurrences and weak updrafts in these levels align with the overall diminishing reflectivity signals depicted in the reflectivity CFADs.

During the early stages of a convective event, VMT is primarily characterized by strong upward mass transport. Occasionally, there may be a combination of strong upward mass transport and subtle net downward transport in the lower levels. These VMT patterns are distinctive markers of the initial convective precipitation phases, highlighting the intensification of convective activity. Furthermore, as the system weakens, we observe larger net downward mass transport resulting from increased evaporational cooling and eventual dissipation due to the influence of stronger horizontally outflowing cold pools.

These changes in VMT patterns are indicative of the later stages of the convective lifecycle, reflecting stratiform activity and the transition towards the dissipation of the system. These observed patterns offer valuable insights into the dynamic behavior of convective systems within each group, enabling the identification and comparison of distinct stages in their life cycles, ultimately enhancing our understanding of the underlying mechanisms, like vertical velocity and vertical moisture flux, driving precipitation trends.

# Chapter 5

## Conclusions

In this study, our objective was to examine the critical ingredients (i.e. stability, moisture, vertical motions) necessary for a heavy precipitation event in northeastern Colorado and assess its predictability across multiple numerical models. We analyzed the thermodynamic, dynamic, and vertical structure of a summertime afternoon storm with a mesoscale convective vortex (MCV) on 30-31 July 2021, utilizing radar-derived precipitation products as well as global and regional model forecast simulations. The GFDL C-SHiELD, an innovative global model with its finest-mesh innermost domain spanning the CONUS, was run six times during the days leading into the selected event; the forecast simulation initialized 36 hours prior to the event was selected as the most representative of the observed conditions for this case. The regional model was the Penn State WRF-EnKF system, which was run as a 20-member ensemble forecast. To assess variability in the ensemble runs, we categorized the WRF ensemble members into three groups ('similar to obs', 'backheavy' and 'simulated MCV') based on their precipitation behavior and MCV formation patterns. By analyzing the agreements and disparities between the models and observations, our ultimate goal was to assess the performance between both "convection-allowing" models in simulating the event and understanding key processes driving simulation variability.

Among the six C-SHiELD forecast simulations, the 36-hour forecast demonstrated a delayed onset of convection and a longer duration compared to other forecasts. Its selection was based on accurately reproducing rainfall rates from the StageIV dataset and successfully simulating an MCV. However, this model's performance before convective initiation (CI) was marked by elevated CIN values, leading to a delayed onset of precipitation compared to observed data. The presence of a stable layer at lower levels acted as a constraining factor, impeding the upward progression of precipitation. The

simulation showcased a notable rise in Potential Vorticity (PV) values associated with the MCV, yet insufficient midlevel humidity hindered the likelihood of convective precipitation, curbing MCV intensification and eventually leading to premature storm dissipation and subsequent dry periods. The observed differences between C-SHiELD 2020 and 2021 could be attributed to modifications in the land surface model parameterization, potentially accounting for the observed low moisture content and precipitation biases in C-SHiELD 2021.

Clear differences emerged in the performance of the WRF and C-SHiELD models. Notably, the WRF ensemble members displayed a higher level of agreement with observed data, particularly concerning the initiation and duration of convection. Although the C-SHiELD precipitation rates were similar to the observations at times, the midlevels were relatively drier and this increased the likelihood of dry air entrainment which limited the convection lifetime. The WRF ensemble simulations displayed a wide range of results, but overall the WRF generally outperformed C-SHiELD by capturing sustained precipitation of the actual event. This enhanced performance can be attributed to several factors, including elevated CAPE and reduced CIN levels around the time of CI, in addition to consistently higher midlevel moisture levels throughout the event.

The three distinct WRF groups also displayed notable differences in their dynamic and kinematic features, primarily influenced by their unique initial conditions which directly shaped their precipitation patterns. The ‘similar to obs’ group closely mirrored observed precipitation rates and was characterized by consistently low CAPE and CIN values. Additionally, this group lacked notable low-level wind shear and maintained a persistent midlevel dry region. The presence of dry-air entrainment posed constraints on the upward Vertical Moisture Flux (VMF) into the midlevels, resulting in reduced precipitation efficiency and subsequently lower reflectivity values. Furthermore, the group’s persistent weak updrafts, particularly at lower levels, further contributed to diminished VMF and provided strong indications of stratiform precipitation.

The ‘backheavy’ group initially resembled the ‘similar to obs’ group with some differences. Both had similar CAPE, low CIN, and a midlevel dry-air region, limiting early rainfall. However, the ‘backheavy’ group had slightly higher CAPE and stronger early-stage updrafts, leading to a higher initial precipitation rate. As the dry pocket dissipated, their precipitation increased due to intensified updrafts and reduced moisture entrainment. They also had low-level wind shear, aiding system progression. Reflectivity patterns showed stronger convective activity, and their convective life cycle resembled

the ‘similar to obs’ group initially but evolved with pronounced peaks in vertical mass transport, indicating stratiform precipitation. This highlights how small differences in initial conditions can lead to distinct outcomes.

The ‘simulated MCV’ group demonstrated heightened precipitation rates relative to observations. This group was distinguished by consistently favorable meteorological conditions, including elevated CAPE, moderate wind shear, low CIN, high PV, and consistently moist midlevels throughout the event’s duration. These favorable conditions contributed to the prolonged convective activity observed in this group, setting it apart from the other two categories. Notably, the ‘simulated MCV’ group exhibited the highest average PV, aligning with the anticipated elevated PV cores associated with MCV phenomena. Additionally, this group displayed the strongest vertical velocity and VMF values during the initial stages, helping sustain precipitation production. While upper-level ice formation paralleled the ‘backheavy’ group, weaker updrafts and VMF in later stages diverged from ‘backheavy’ characteristics, resulting in increased net downward mass transport and eventual system decay.

A key finding of this study is the discernible difference in performance between the WRF and C-SHiELD models. Given their distinct parameterizations and approaches, it was essential to compare these models to evaluate their ability to simulate a nominal precipitation event. C-SHiELD’s initial conditions, derived from Global Forecasting System (GFS) data, exhibited higher accuracy in short-term forecasts but showed reduced reliability with extended lead times due to evolving atmospheric conditions and inherent uncertainties. Specifically, the 36-hour forecast proved less accurate in predicting the onset and duration of precipitation in comparison to both StageIV and WRF. This discrepancy primarily stemmed from the model’s early-phase representation of an atmosphere characterized by excessively high low-level stability and insufficient midlevel moisture levels throughout the event. These findings emphasize the necessity for a comprehensive assessment of multiple C-SHiELD model forecasts and warrant further exploration into potential adjustments related to land-surface parameterization. Such endeavors would offer valuable insights into the stability and consistency of the variables under examination. Furthermore, the commendable performance of the WRF model accentuates its potential for future ensemble forecasting initiatives.

Another major finding of this research pertains to the performance of the ‘similar to obs’ ensemble group. This group exhibited an exceptional level of agreement with observed data, primarily attributed to the prominent presence of a midlevel dry air

pocket as indicated in the Denver sounding profile, which limited precipitation efficiency. Nevertheless, it did not replicate the observed MCV phenomenon in the same manner as the ‘simulated MCV’ group. Given that the ‘simulated MCV’ group generally outperformed in terms of precipitation rates, these discrepancies may be ascribed to inaccuracies within the model’s microphysical processes or the initial environmental state. Similar precipitation disparities were observed in the ‘backheavy’ group, further supporting this notion. The precise capture of intricate factors influencing precipitation rates, vertical moisture profiles, and MCV simulation remains a formidable challenge, necessitating a comprehensive examination of the diverse modeling schemes employed. Differences between the three WRF groups underscore their distinct characteristics corresponding to anticipated dynamics and thermodynamics within the prevailing environmental conditions, highlighting the pivotal role of accurate environmental factor initialization in achieving reliable WRF forecasts.

While this study provides valuable insights into the specific event analyzed, it is important to acknowledge some limitations and areas for future exploration. The analysis of radar data from CSU-CHILL, CSU-CHIVO, and S-Pol was not included in this study, and incorporating radar data analysis in future research could shed light on additional meteorological phenomena related to storm motion and precipitation type. Exploring these aspects can contribute to a more comprehensive understanding of the forecasting process. The StageIV dataset could have also been re-gridded for more accurate grid-scale comparisons. Furthermore, performing additional investigations on a broader range of C-SHiELD forecasts is essential to identify potential variations in environmental conditions and evaluate the accuracy of the model. Additionally, conducting in-depth analyses of the vertical structures within the C-SHiELD output would provide valuable insights into the spatial distribution of crucial thermodynamic, kinematic and dynamic variables. Finally, our ensemble separation technique was inspired by similar techniques from previous studies, and can potentially be extended in scope for future studies, as it can be utilized to uncover additional variability among distinct groups with different behaviors. Exploring alternative methodologies for grouping ensemble members, such as considering their initial conditions, could yield additional valuable insights into precipitation intensity and duration that would emerge later in the system’s lifetime. By closely examining the fundamental elements necessary for CI, we can enhance the accuracy of heavy precipitation forecasts, thus improving our ability to predict and understand such events across diverse climatic conditions.

# Bibliography

- Barkidija, S. and Z. Fuchs, 2013: Precipitation correlation between convective available potential energy, convective inhibition and saturation fraction in middle latitudes. *Atmospheric Research*, **124**, 170–180, doi:10.1016/j.atmosres.2012.12.010.  
URL <https://www.sciencedirect.com/science/article/pii/S0169809513000045?via%3Dihub#bb0065>
- Bartels, D. L. and R. A. Maddox, 1991: Midlevel cyclonic vortices generated by mesoscale convective systems. *Monthly Weather Review*, **119**, 104–118, doi:10.1175/1520-0493(1991)119<0104:MCVGBM>2.0.CO;2.  
URL [https://journals.ametsoc.org/view/journals/mwre/119/1/1520-0493\\_1991\\_119\\_0104\\_mcvgbm\\_2\\_0\\_co\\_2.xml](https://journals.ametsoc.org/view/journals/mwre/119/1/1520-0493_1991_119_0104_mcvgbm_2_0_co_2.xml)
- Bernardet, P., 1995: The pressure term in the anelastic model: A symmetric elliptic solver for an arakawa c grid in generalized coordinates. *Monthly Weather Review*, **123**, 2474–2490, doi:10.1175/1520-0493(1995)123<2474:TPTITA>2.0.CO;2.  
URL [https://journals.ametsoc.org/view/journals/mwre/123/8/1520-0493\\_1995\\_123\\_2474\\_tptita\\_2\\_0\\_co\\_2.xml](https://journals.ametsoc.org/view/journals/mwre/123/8/1520-0493_1995_123_2474_tptita_2_0_co_2.xml)
- Bosart, L. F. and F. Sanders, 1981: The johnstown flood of july 1977: A long-lived convective system. *Journal of the Atmospheric Sciences*, **38**, 1616–1642, doi:10.1175/1520-0469(1981)038<1616:TJFOJA>2.0.CO;2.  
URL [https://journals.ametsoc.org/view/journals/atsc/38/8/1520-0469\\_1981\\_038\\_1616\\_tjfoja\\_2\\_0\\_co\\_2.xml](https://journals.ametsoc.org/view/journals/atsc/38/8/1520-0469_1981_038_1616_tjfoja_2_0_co_2.xml)
- Bronstert, A., 2003: Floods and climate change: Interactions and impacts. *Risk Analysis*, **23**, 545–557, doi:10.1111/1539-6924.00335.  
URL [https://onlinelibrary.wiley.com/doi/full/10.1111/1539-6924.00335?casa\\_token=YjaQB9kVUCEAAAAA\%3AmwK22IzQhVclgYR9Ubo-vkwXaC6AGbEx3tmdLBqmrw7gpiV2ZY-kHhqtFxbzLhAQ0so4Cry\\_g3hPrtw](https://onlinelibrary.wiley.com/doi/full/10.1111/1539-6924.00335?casa_token=YjaQB9kVUCEAAAAA\%3AmwK22IzQhVclgYR9Ubo-vkwXaC6AGbEx3tmdLBqmrw7gpiV2ZY-kHhqtFxbzLhAQ0so4Cry_g3hPrtw)
- Brooks, H. E., A. R. Anderson, K. Riemann, I. Ebberts, and H. Flachs, 2007: The spatial distribution of severe thunderstorm and tornado environments from global reanalysis data. *Atmospheric Research*, **83**, 294–305, doi:10.1016/j.atmosres.2005.08.005.

- URL <https://www.sciencedirect.com/science/article/pii/S0169809506001128>
- Brooks, H. E., J. W. Lee, and J. P. Craven, 2003: The spatial distribution of severe thunderstorm and tornado environments from global reanalysis data. *Atmospheric Research*, **67**, 73–94, doi:10.1016/S0169-8095(03)00045-0.  
URL <https://www.sciencedirect.com/science/article/pii/S0169809503000450>
- Bryan, G. H., J. C. Wyngaard, and J. M. Fritsch, 2003: Resolution requirements for the simulation of deep moist convection. *Monthly Weather Review*, **131**, 2394–2416, doi:10.1175/1520-0493(2003)131<2394:RRFTSO>2.0.CO;2.  
URL [https://journals.ametsoc.org/view/journals/mwre/131/10/1520-0493\\_2003\\_131\\_2394\\_rrftso\\_2.0.co\\_2.xml](https://journals.ametsoc.org/view/journals/mwre/131/10/1520-0493_2003_131_2394_rrftso_2.0.co_2.xml)
- Cannon, S. H., J. E. Gartner, R. C. Wilson, J. C. Bowers, and J. L. Laber, 2008: Storm rainfall conditions for floods and debris flows from recently burned areas in southwestern colorado and southern california. *Geomorphology*, **96**, 250–269, doi:10.1016/j.geomorph.2007.03.019.  
URL [https://www.sciencedirect.com/science/article/pii/S0169555X07001778?casa\\_token=R3BJLMP1E9cAAAAA:nUtI5s1yiEC7r7-4wJGKXif6cSqPHP0yhULDJk-1eKkDgmwT3DZhHKG0okodv7uXVZqPdie7kIs](https://www.sciencedirect.com/science/article/pii/S0169555X07001778?casa_token=R3BJLMP1E9cAAAAA:nUtI5s1yiEC7r7-4wJGKXif6cSqPHP0yhULDJk-1eKkDgmwT3DZhHKG0okodv7uXVZqPdie7kIs)
- Chan, M.-Y., F. Zhang, X. Chen, and L. R. Leung, 2020: Potential impacts of assimilating all-sky satellite infrared radiances on convection-permitting analysis and prediction of tropical convection. *Monthly Weather Review*, **148**, 3203–3224, doi:10.1175/MWR-D-19-0343.1.  
URL <https://journals.ametsoc.org/view/journals/mwre/148/8/mwrD190343.xml>
- Chen, Q., J. Fan, S. Hagos, W. I. G. Jr., and L. K. Berg, 2015: Roles of wind shear at different vertical levels: Cloud system organization and properties. *JGR Atmospheres*, **120**, 6551–6574, doi:10.1002/2015JD023253.  
URL <https://agupubs.onlinelibrary.wiley.com/doi/full/10.1002/2015JD023253>
- Chen, T., J. Guo, Z. Li, C. Zhao, H. Liu, M. Cribb, F. Wang, , and J. He, 2016: A cloudsat perspective on the cloud climatology and its association with aerosol perturbations in the vertical over eastern china. *Journal of the Atmospheric Sciences*, **73**, 3599–3616, doi:10.1175/JAS-D-15-0309.1.  
URL <https://journals.ametsoc.org/view/journals/atsc/73/9/jas-d-15-0309.1.xml>
- Chen, X. and F. Zhang, 2019: Development of a convection-permitting air-sea-coupled ensemble data assimilation system for tropical cyclone prediction. *AGU Advances*, **11**,

- doi:10.1029/2019MS001795.  
URL <https://agupubs.onlinelibrary.wiley.com/doi/10.1029/2019ms001795>
- Conzemius, R. J. and M. T. Montgomery, 2009: Clarification on the generation of absolute and potential vorticity in mesoscale convective vortices. **9**, doi:10.5194/acp-9-7591-2009.  
URL <https://acp.copernicus.org/articles/9/7591/2009/>
- Craven, J., H. Brooks, and J. Hart, 2002: Baseline climatology of sounding derived parameters associated with deep moist convection. *Preprints, 21st Conference on Severe Local Storms*, 643–646.  
URL <https://citeseerx.ist.psu.edu/document?repid=rep1&type=pdf&doi=ec3c3202c0f3de047d7dc3b49a2a429b21da5a23>
- Dai, A., F. Giorgi, and K. E. Trenberth, 1999: Observed and model-simulated diurnal cycles of precipitation over the contiguous united states. *Journal of Geophysical Research: Atmospheres*, **104**, 6377–6402, doi:10.1029/98JD02720.  
URL <https://agupubs.onlinelibrary.wiley.com/doi/10.1029/98JD02720>
- Demeritt, D., H. Cloke, F. Pappenberger, J. Thielen, J. Bartholmes, and M.-H. Ramos, 2007: Ensemble predictions and perceptions of risk, uncertainty, and error in flood forecasting. *Environmental Hazards*, **7**, 115–127, doi:10.1016/j.envhaz.2007.05.001.  
URL <https://www.sciencedirect.com/science/article/abs/pii/S1747789107000117>
- Didlake, A. C. and R. A. Houze, 2013: Dynamics of the Stratiform Sector of a Tropical Cyclone Rainband. *Journal of the Atmospheric Sciences*, **70**, 1891–1911, doi:10.1175/JAS-D-12-0245.1.
- Dirks, R., 1969: A theoretical investigation of convective patterns in the lee of the colorado rockies, 12–134.  
URL [https://mountainscholar.org/bitstream/handle/10217/243/0154\\_Bluebook.pdf?sequence=1&isAllowed=y](https://mountainscholar.org/bitstream/handle/10217/243/0154_Bluebook.pdf?sequence=1&isAllowed=y)
- Done, J., C. A. Davis, and M. Weisman, 2004: The next generation of nwp: explicit forecasts of convection using the weather research and forecasting (wrf) model. *Royal Meteorological Society*, **5**, 110–117, doi:10.1002/asl.72.  
URL <https://rmets.onlinelibrary.wiley.com/doi/10.1002/asl.72>
- Doswell, C. A., 1986: The distinction between large-scale and mesoscale contribution to severe convection: A case study example. *Weather and Forecasting*, **2**, 3–16, doi:10.1175/1520-0434(1987)002<0003:TDBLSA>2.0.CO;2.

- URL [https://journals.ametsoc.org/view/journals/wefo/2/1/1520-0434\\_1987\\_002\\_0003\\_tdblsa\\_2\\_0\\_co\\_2.xml?tab\\_body=pdf](https://journals.ametsoc.org/view/journals/wefo/2/1/1520-0434_1987_002_0003_tdblsa_2_0_co_2.xml?tab_body=pdf)
- Doswell, C. A., H. E. Brooks, and R. A. Maddox, 1996: Flash flood forecasting: An ingredients-based methodology. *Weather and Forecasting*, **11**, 560–581, doi:10.1175/1520-0434(1996)011<0560:FFFAIB>2.0.CO;2.  
URL [https://journals.ametsoc.org/view/journals/wefo/11/4/1520-0434\\_1996\\_011\\_0560\\_fffaib\\_2\\_0\\_co\\_2.xml](https://journals.ametsoc.org/view/journals/wefo/11/4/1520-0434_1996_011_0560_fffaib_2_0_co_2.xml)
- Doswell, C. A. and J. S. Evans, 2003: Proximity sounding analysis for derechos and supercells: an assessment of similarities and differences. *Atmospheric Research*, **67**, 117–133, doi:10.1016/S0169-8095(03)00047-4.  
URL <https://www.sciencedirect.com/science/article/pii/S0169809503000474>
- Dougherty, E. and K. L. Rasmussen, 2020: Changes in future flash flood-producing storms in the united states. *Journal of Hydrometeorology*, **21**, 2221–2236, doi:10.1175/JHM-D-20-0014.1.  
URL <https://journals.ametsoc.org/view/journals/hydr/21/10/jhmD200014.xml#bib63>
- Emanuel, K. A., 1994: *Atmospheric Convection*. Oxford University Press.  
URL [https://books.google.com/books?hl=en&lr=&id=VdaBBHEGAcMC&oi=fnd&pg=PA3&ots=WBs1qFqrGc&sig=8cNN44xMJw7ie4tEQc\\_c08v7ZIIY#v=onepage&q&f=false](https://books.google.com/books?hl=en&lr=&id=VdaBBHEGAcMC&oi=fnd&pg=PA3&ots=WBs1qFqrGc&sig=8cNN44xMJw7ie4tEQc_c08v7ZIIY#v=onepage&q&f=false)
- Flora, M. L., P. S. Skinner, C. K. Potvin, A. E. Reinhart, T. A. Jones, N. Yussouf, and K. H. Knopfmeier, 2019: Storm-scale data assimilation and ensemble forecasting with the nssl experimental warn-on-forecast system. part ii: Combined radar and satellite data experiments. *Weather and Forecasting*, **34**, 1721–1739, doi:10.1175/WAF-D-19-0094.1.  
URL [https://journals.ametsoc.org/view/journals/wefo/34/6/waf-d-19-0094\\_1.xml](https://journals.ametsoc.org/view/journals/wefo/34/6/waf-d-19-0094_1.xml)
- Fovell, R. G. and Y. Ogura, 1989: Effect of vertical wind shear on numerically simulated multicell storm structure. *Journal of the Atmospheric Sciences*, **46**, 3144–3176, doi:10.1175/1520-0469(1989)046<3144:EOVWSO>2.0.CO;2.  
URL [https://journals.ametsoc.org/view/journals/atsc/46/20/1520-0469\\_1989\\_046\\_3144\\_eovwso\\_2\\_0\\_co\\_2.xml](https://journals.ametsoc.org/view/journals/atsc/46/20/1520-0469_1989_046_3144_eovwso_2_0_co_2.xml)
- Fox, D., Y. Laaroussi, L. Malkinson, F. Maselli, J. Andrieu, L. Bottai, and L. Wittenberg, 2016: Postfire: A model to map forest fire burn scar and estimate runoff and soil erosion risks. *Remote Sensing Applications: Society and Environment*, **4**, 83–91, doi:10.1016/j.rsase.2016.07.002.

URL <https://www.sciencedirect.com/science/article/abs/pii/S2352938516300313>

Friedrich, K., E. A. Kalina, J. Aikins, D. Gochis, and R. Rasmussen, 2016: Precipitation and cloud structures of intense rain during the 2013 great colorado flood. *Journal of Hydrometeorology*, **17**, 27–52, doi:10.1175/JHM-D-14-0157.1.

URL [https://journals.ametsoc.org/view/journals/hydr/17/1/jhm-d-14-0157\\_1.xml?tab\\_body=fulltext-display](https://journals.ametsoc.org/view/journals/hydr/17/1/jhm-d-14-0157_1.xml?tab_body=fulltext-display)

Fritsch, J. M., R. J. Kane, and C. R. Chelius, 1986: The contribution of mesoscale convective weather systems to the warm-season precipitation in the united states. *Journal of Applied Meteorology and Climatology*, **25**, 1333–1345, doi:10.1175/1520-0450(1986)025<1333:TCOMCW>2.0.CO;2.

URL [https://journals.ametsoc.org/view/journals/apme/25/10/1520-0450\\_1986\\_025\\_1333\\_tcomcw\\_2\\_0\\_co\\_2.xml#:~:text=It%20is%20found%20that%20mesoscale,Mountains%20and%20the%20Mississippi%20River.](https://journals.ametsoc.org/view/journals/apme/25/10/1520-0450_1986_025_1333_tcomcw_2_0_co_2.xml#:~:text=It%20is%20found%20that%20mesoscale,Mountains%20and%20the%20Mississippi%20River.)

Fritsch, J. M., J. D. Murphy, and J. S. Kain, 1994: Warm core vortex amplification over land. *Journal of the Atmospheric Sciences*, **51**, 1780–1807, doi:10.1175/1520-0469(1994)051<1780:WCVAOL>2.0.CO;2.

URL [https://journals.ametsoc.org/view/journals/atsc/51/13/1520-0469\\_1994\\_051\\_1780\\_wcvaol\\_2\\_0\\_co\\_2.xml](https://journals.ametsoc.org/view/journals/atsc/51/13/1520-0469_1994_051_1780_wcvaol_2_0_co_2.xml)

Galarneau, T. J., L. J. Wicker, K. H. Knopfmeier, W. J. S. Miller, P. S. Skinner, and K. A. Wilson, 2022: Short-term prediction of a nocturnal significant tornado outbreak using a convection-allowing ensemble. *Weather and Forecasting*, **37**, 1027–1047, doi:10.1175/WAF-D-21-0160.1.

URL <https://journals.ametsoc.org/view/journals/wefo/37/6/WAF-D-21-0160.1.xml>

GFDL, 2021: C-SHiELD - Continental System for High Resolution Prediction on Earth-to-Local Domains.

URL <https://www.gfdl.noaa.gov/shield/#C-SHiELD>

Gochis, D., R. Schumacher, K. Friedrich, N. Doesken, M. Kelsch, J. Sun, K. Ikeda, D. Lindsey, A. Wood, B. Dolan, S. Matrosov, A. Newman, K. Mahoney, S. Rutledge, R. Johnson, P. Kucera, P. Kennedy, D. Sempere-Torres, M. Steiner, R. Roberts, J. Wilson, W. Yu, V. Chandrasekar, R. Rasmussen, A. Anderson, and B. Brown, 2015: The great colorado flood of september 2013. *Bulletin of the American Meteorological Society*, **96**, 1461–1487, doi:10.1175/BAMS-D-13-00241.1.

URL <https://journals.ametsoc.org/view/journals/bams/96/9/bams-d-13-00241.1.xml>

- Gray, K. and J. Frame, 2019: Investigating the transition from elevated multicellular convection to surface-based supercells during the tornado outbreak of 24 august 2016 using a wrf model simulation. *Weather and Forecasting*, **34**, 3144–3176, doi:10.1175/WAF-D-18-0209.1.  
URL [https://journals.ametsoc.org/view/journals/wefo/34/4/waf-d-18-0209\\_1.xml](https://journals.ametsoc.org/view/journals/wefo/34/4/waf-d-18-0209_1.xml)
- Han, J. and C. S. Bretherton, 2019: Tke-based moist eddy-diffusivity mass-flux (edmf) parameterization for vertical turbulent mixing. *Weather and Forecasting*, **34**, 869–886, doi:10.1175/WAF-D-18-0146.1.  
URL [https://journals.ametsoc.org/view/journals/wefo/34/4/waf-d-18-0146\\_1.xml](https://journals.ametsoc.org/view/journals/wefo/34/4/waf-d-18-0146_1.xml)
- Han, J., W. Wang, Y. C. Kwon, S.-Y. Hong, V. Tallapragada, and F. Yang, 2017: Updates in the ncep gfs cumulus convection schemes with scale and aerosol awareness. *Weather and Forecasting*, **32**, 2005–2017, doi:10.1175/WAF-D-17-0046.1.  
URL [https://journals.ametsoc.org/view/journals/wefo/32/5/waf-d-17-0046\\_1.xml](https://journals.ametsoc.org/view/journals/wefo/32/5/waf-d-17-0046_1.xml)
- Harris, L., X. Chen, Z. Liang, J. Chen, and W. M. Putman, 2021: A scientific description of the gfdl finite-volume cubed-sphere dynamical core. *Journal of Advanced Earth and Space Science*, doi:10.25923/6nhs-5897.  
URL <https://repository.library.noaa.gov/view/noaa/30725>
- Harris, L. and S.-J. Lin, 2013: A two-way nested global-regional dynamical core on the cubed-sphere grid. *Monthly Weather Review*, **141**, 283–306, doi:10.1175/MWR-D-11-00201.1.  
URL <https://journals.ametsoc.org/view/journals/mwre/141/1/mwr-d-11-00201.1.xml>
- Harris, L., L. Zhou, S. Lin, J. Chen, X. Chen, K. Gao, M. Morin, S. Rees, Y. Sun, M. Tong, B. Xiang, M. Bender, R. Benson, K. Cheng, S. Clark, O. Elbert, A. Hazelton, J. Huff, A. Kaltenbaugh, Z. Liang, T. Marchok, H. Shin, and W. Stern, 2020: Gfdl shield: A unified system for weather-to-seasonal prediction. *Journal of Advanced Earth and Space Science*, **12**, 55–78, doi:10.1029/2020MS002223.  
URL <https://agupubs.onlinelibrary.wiley.com/doi/10.1029/2020MS002223>
- Haynes, P. H. and M. E. McIntyre, 1987: On the evolution of vorticity and potential vorticity in the presence of diabatic heating and frictional or other forces. *Journal of the Atmospheric Sciences*, **44**, 828–841, doi:10.1175/1520-0469(1987)044<0828:OTEOVA>2.0.CO;2.  
URL [https://journals.ametsoc.org/view/journals/atsc/44/5/1520-0469\\_1987\\_044\\_0828\\_oteova\\_2\\_0\\_co\\_2.xml](https://journals.ametsoc.org/view/journals/atsc/44/5/1520-0469_1987_044_0828_oteova_2_0_co_2.xml)

- Henz, J., 1973: Characteristics of severe convective storms on colorado's high plains. *Preprints, 8th Conference on Severe Local Storms*, 96–103.
- Hirabayashi, Y., R. Mahendran, S. Koirala, L. Konoshima, D. Yamazaki, S. Watanabe, H. Kim, and S. Kanae, 2013: Global flood risk under climate change. *Nature Climate Change*, **119**, 104–118.
- Houze, R. A., 1997: Stratiform precipitation in regions of convection: A meteorological paradox? *Bulletin of the American Meteorological Society*, **78**, 2179 – 2196, doi:10.1175/1520-0477(1997)078<2179:SPIROC>2.0.CO;2.  
URL [https://journals.ametsoc.org/view/journals/bams/78/10/1520-0477\\_1997\\_078\\_2179\\_spiroc\\_2\\_0\\_co\\_2.xml](https://journals.ametsoc.org/view/journals/bams/78/10/1520-0477_1997_078_2179_spiroc_2_0_co_2.xml)
- 2004: Mesoscale convective systems. *Journal of Geophysical Research: Atmospheres*, **42**, 6377–6402, doi:10.1029/2004RG000150.  
URL <https://agupubs.onlinelibrary.wiley.com/doi/10.1029/2004RG000150>
- Huang, Y., A. Protat, S. T. Siems, and M. J. Manton, 2015: A-train observations of maritime midlatitude storm-track cloud systems: Comparing the southern ocean against the north atlantic. *Journal of the Atmospheric Sciences*, **28**, 1920–1939, doi:10.1175/JCLI-D-14-00169.1.  
URL <https://journals.ametsoc.org/view/journals/clim/28/5/jcli-d-14-00169.1.xml>
- Jones, T. A., K. Knopfmeier, D. Wheatley, G. Creager, P. Minnis, and R. Palikonda, 2016: Storm-scale data assimilation and ensemble forecasting with the nssl experimental warn-on-forecast system. part ii: Combined radar and satellite data experiments. *Weather and Forecasting*, **31**, 297–327, doi:10.1175/WAF-D-15-0107.1.  
URL [https://journals.ametsoc.org/view/journals/wefo/31/1/waf-d-15-0107\\_1.xml](https://journals.ametsoc.org/view/journals/wefo/31/1/waf-d-15-0107_1.xml)
- Junker, N. W., R. S. Schneider, and S. L. Fauver, 1999: A study of heavy rainfall events during the great midwest flood of 1993. *Weather and Forecasting*, **14**, 701–712, doi:10.1175/1520-0434(1999)014<0701:ASOHRE>2.0.CO;2.  
URL [https://journals.ametsoc.org/view/journals/wefo/14/5/1520-0434\\_1999\\_014\\_0701\\_asohre\\_2\\_0\\_co\\_2.xml](https://journals.ametsoc.org/view/journals/wefo/14/5/1520-0434_1999_014_0701_asohre_2_0_co_2.xml)
- Kaltenbaugh, A., L. Harris, K.-Y. Cheng, L. Zhou, M. Morin, and W. Stern, 2022: Using gfdl c-shield for the prediction of convective storms during the 2021 spring and summe.  
URL <https://repository.library.noaa.gov/view/noaa/43729>
- Karr, T. W. and R. L. Wooten, 1976: Summer radar echo distribution around limon, colorado. *Monthly Weather Review*, **104**, 728–734, doi:10.1175/1520-0493(1976)104<0728:SREDAL>2.0.CO;2.

- URL [https://journals.ametsoc.org/view/journals/mwre/104/6/1520-0493\\_1976\\_104\\_0728\\_sredal\\_2\\_0\\_co\\_2.xml](https://journals.ametsoc.org/view/journals/mwre/104/6/1520-0493_1976_104_0728_sredal_2_0_co_2.xml)
- Klotzbach, P. J., S. G. Bowen, R. Pielke Jr., and M. Bell, 2018: Continental u.s. hurricane landfall frequency and associated damage: Observations and future risks. *Journal of Climate*, **99**, 1359–1376, doi:10.1175/BAMS-D-17-0184.1.  
URL <https://journals.ametsoc.org/view/journals/bams/99/7/bams-d-17-0184.1.xml>
- Knievel, J. C., 2001: Kinematics and thermodynamics of a midlatitude, continental mesoscale convective system and its mesoscale vortex. **21**.  
URL <https://ezaccess.libraries.psu.edu/login?url=https://www.proquest.com/dissertations-theses/kinematics-thermodynamics-midlatitude-continental/docview/275686406/se-2>
- Lin, S.-J., 2004: A “vertically lagrangian” finite-volume dynamical core for global models. *Monthly Weather Review*, **132**, 2293–2307, doi:10.1175/1520-0493(2004)132<2293:AVLFDC>2.0.CO;2.  
URL [https://journals.ametsoc.org/view/journals/mwre/132/10/1520-0493\\_2004\\_132\\_2293\\_avlfdc\\_2.0\\_co\\_2.xml](https://journals.ametsoc.org/view/journals/mwre/132/10/1520-0493_2004_132_2293_avlfdc_2.0_co_2.xml)
- Lopez, R. E. and R. L. Holle, 1986: Diurnal and spatial variability of lightning activity in northeastern colorado and central florida during the summer. *Monthly Weather Review*, **114**, 1288–1312, doi:10.1175/1520-0493(1986)114<1288:DASVOL>2.0.CO;2.  
URL [https://journals.ametsoc.org/view/journals/mwre/114/7/1520-0493\\_1986\\_114\\_1288\\_dasvol\\_2\\_0\\_co\\_2.xml?tab\\_body=pdf](https://journals.ametsoc.org/view/journals/mwre/114/7/1520-0493_1986_114_1288_dasvol_2_0_co_2.xml?tab_body=pdf)
- Maddox, R. A., C. F. Chappell, and L. R. Hoxit, 1999: Synoptic and meso- scale aspects of flash flood events. **60**, 115–123.  
URL <http://www.jstor.org/stable/26219020>.
- Marion, G. R. and R. J. Trapp, 2018: The dynamical coupling of convective updrafts, downdrafts, and cold pools in simulated supercell thunderstorms. *JGR Atmospheres*, **120**, 664–683, doi:10.1029/2018JD029055.  
URL <https://agupubs.onlinelibrary.wiley.com/doi/full/10.1029/2018JD029055>
- Markowski, P. M., J. M. Straka, and E. N. Rasmussen, 2002: Direct surface thermodynamic observations within the rear-flank downdrafts of nontornadic and tornadic supercells. *Monthly Weather Review*, **130**, 1692–1721, doi:10.1175/1520-0493(2002)130<1692:DSTOWT>2.0.CO;2.  
URL [https://journals.ametsoc.org/view/journals/mwre/130/7/1520-0493\\_2002\\_130\\_1692\\_dstowt\\_2.0\\_co\\_2.xml?tab\\_body=fulltext-display](https://journals.ametsoc.org/view/journals/mwre/130/7/1520-0493_2002_130_1692_dstowt_2.0_co_2.xml?tab_body=fulltext-display)

- Masunaga, H., M. Satoh, and H. Miura, 2008: A joint satellite and global cloud-resolving model analysis of a madden-julian oscillation event: Model diagnosis. *Aerosol and Clouds*, **113**, doi:10.1029/2008JD009986.  
URL <https://agupubs.onlinelibrary.wiley.com/doi/full/10.1029/2008JD009986>
- Merwade, V., A. Cook, and J. Coonrod, 2008: Gis techniques for creating river terrain models for hydrodynamic modeling and flood inundation mapping. *Environmental Modelling Software*, **23**, 1300–1311, doi:10.1016/j.envsoft.2008.03.005.  
URL <https://www.sciencedirect.com/science/article/abs/pii/S1364815208000455>
- Moore, J. T., F. H. Glass, C. E. Graves, S. M. Rochette, and M. J. Singer, 2003: The environment of warm-season elevated thunderstorms associated with heavy rainfall over the central united states. *Weather and Forecasting*, **18**, 861–878, doi:10.1175/1520-0434(2003)018<0861:TEOWET>2.0.CO;2.  
URL [https://journals.ametsoc.org/view/journals/wefo/18/5/1520-0434\\_2003\\_018\\_0861\\_teowet\\_2\\_0\\_co\\_2.xml](https://journals.ametsoc.org/view/journals/wefo/18/5/1520-0434_2003_018_0861_teowet_2_0_co_2.xml)
- Morrison, H., 2017: An analytic description of the structure and evolution of growing deep cumulus updrafts. *Journal of the Atmospheric Sciences*, **74**, 809–834, doi:10.1175/JAS-D-16-0234.1.  
URL <https://journals.ametsoc.org/view/journals/atsc/74/3/jas-d-16-0234.1.xml>
- Morrison, H., J. M. Peters, A. C. Varble, W. M. Hannah, and S. E. Giangrande, 2020a: Thermal chains and entrainment in cumulus updrafts. part i: Theoretical description. *Journal of the Atmospheric Sciences*, **77**, 3637–3660, doi:10.1175/JAS-D-19-0243.1.  
URL <https://journals.ametsoc.org/view/journals/atsc/77/11/JAS-D-19-0243.1.xml>
- Morrison, H., M. van Lier-Walqui, A. M. Fridlind, W. W. Grabowski, J. Y. Harrington, C. Hoose, A. Korolev, M. R. Kumjian, J. A. Milbrandt, H. Pawlowska, D. J. Posselt, O. P. Prat, K. J. Reimel, S.-I. Shima, B. van Dierenhoven, and L. Xue, 2020b: Confronting the challenge of modeling cloud and precipitation microphysics. *Journal of Advanced Earth and Space Science*, **12**, doi:10.1029/2019MS001689.  
URL <https://agupubs.onlinelibrary.wiley.com/doi/full/10.1029/2019MS001689>
- Morton, B. R., G. Taylor, and J. S. Turner, 1956: Turbulent gravitational convection from maintained and instantaneous sources. **234**, 1–23.  
URL <https://www.jstor.org/stable/99936>
- Mulholland, J. P., J. M. Peters, and H. Morrison, 2021: How does vertical wind shear influence entrainment in squall lines? *Journal of the Atmospheric Sciences*, **78**,

- 1931–1946, doi:10.1175/JAS-D-20-0299.1.  
 URL <https://journals.ametsoc.org/view/journals/atsc/78/6/JAS-D-20-0299.1.xml>
- Nelson, B. R., O. P. Prat, D.-J. Seo, and E. Habib, 2016: Assessment and implications of ncep stage iv quantitative precipitation estimates for product intercomparisons. *Weather and Forecasting*, **31**, 371–394, doi:10.1175/WAF-D-14-00112.1.  
 URL <https://journals.ametsoc.org/view/journals/wefo/31/2/waf-d-14-00112.1.xml>
- Peters, J. M., C. J. Nowotarski, and G. L. Mullendore, 2020: Are supercells resistant to entrainment because of their rotation? *Journal of the Atmospheric Sciences*, **77**, 1475–1495, doi:10.1175/JAS-D-19-0316.1.  
 URL <https://journals.ametsoc.org/view/journals/atsc/77/4/jas-d-19-0316.1.xml>
- Pielke, R. and M. W. Downton, 2000: Precipitation and Damaging Floods: Trends in the United States, 1932–97. *Journal of Climate*, **13**, 3625–3637, doi:10.1175/1520-0442(2000)013<3625:PADFTI>2.0.CO;2.  
 URL [https://journals.ametsoc.org/view/journals/clim/13/20/1520-0442\\_2000\\_013\\_3625\\_padfti\\_2.0.co\\_2.xml](https://journals.ametsoc.org/view/journals/clim/13/20/1520-0442_2000_013_3625_padfti_2.0.co_2.xml)
- Putman, W. M. and S.-J. Lin, 2007: Finite-volume transport on various cubed-sphere grids. *Atmospheric Research*, **227**, 55–78, doi:10.1016/j.jcp.2007.07.022.  
 URL <https://www.sciencedirect.com/science/article/pii/S0021999107003105?via3Dihub>
- Rasmussen, E. N. and D. O. Blanchard, 1998: A baseline climatology of sounding-derived supercell and tornado forecast parameters. *Weather and Forecasting*, **13**, 1148–1164, doi:10.1175/1520-0434(1998)013<1148:ABCOSD>2.0.CO;2.  
 URL [https://journals.ametsoc.org/view/journals/wefo/13/4/1520-0434\\_1998\\_013\\_1148\\_abcosd\\_2\\_0\\_co\\_2.xml?tab\\_body=abstract-display](https://journals.ametsoc.org/view/journals/wefo/13/4/1520-0434_1998_013_1148_abcosd_2_0_co_2.xml?tab_body=abstract-display)
- Raymond, D. J. and H. Jiang, 1987: A theory for long-lived mesoscale convective systems. *Journal of the Atmospheric Sciences*, **47**, 3067–3077, doi:10.1175/1520-0469(1990)047<3067:ATFLLM>2.0.CO;2.  
 URL [https://journals.ametsoc.org/view/journals/atsc/47/24/1520-0469\\_1990\\_047\\_3067\\_atflm\\_2\\_0\\_co\\_2.xml](https://journals.ametsoc.org/view/journals/atsc/47/24/1520-0469_1990_047_3067_atflm_2_0_co_2.xml)
- Riemann-Campe, K., K. Fraedrich, and F. Lunkeit, 2009: Global climatology of convective available potential energy (cape) and convective inhibition (cin) in era-40 reanalysis. *Atmospheric Research*, **93**, 534–545, doi:10.1016/j.atmosres.2008.09.037.  
 URL <https://www.sciencedirect.com/science/article/abs/pii/S0169809508002706>

- Riley, G. T., M. G. Landin, and L. F. Bosart, 1987: The diurnal variability of precipitation across the central rockies and adjacent great plains. *Monthly Weather Review*, **115**, 1161–1172, doi:10.1175/1520-0493(1987)115<1161:TDVOPA>2.0.CO;2.  
 URL [https://journals.ametsoc.org/view/journals/mwre/115/6/1520-0493\\_1987\\_115\\_1161\\_tdvopa\\_2\\_0\\_co\\_2.xml](https://journals.ametsoc.org/view/journals/mwre/115/6/1520-0493_1987_115_1161_tdvopa_2_0_co_2.xml)
- Rotunno, R. and J. B. Klemp, 1982: The influence of the shear-induced pressure gradient on thunderstorm motion. *Monthly Weather Review*, **110**, 136–151, doi:10.1175/1520-0493(1982)110<0136:TIOTSI>2.0.CO;2.  
 URL [https://journals.ametsoc.org/view/journals/mwre/110/2/1520-0493\\_1982\\_110\\_0136\\_tioticsi\\_2\\_0\\_co\\_2.xml](https://journals.ametsoc.org/view/journals/mwre/110/2/1520-0493_1982_110_0136_tioticsi_2_0_co_2.xml)
- Rotunno, R., J. B. Klemp, and M. L. Weisman, 1988: A theory for strong, long-lived squall lines. *Journal of the Atmospheric Sciences*, **45**, 463–485, doi:10.1175/1520-0469(1988)045<0463:ATFSSL>2.0.CO;2.  
 URL [https://journals.ametsoc.org/view/journals/atsc/45/3/1520-0469\\_1988\\_045\\_0463\\_atfsll\\_2\\_0\\_co\\_2.xml](https://journals.ametsoc.org/view/journals/atsc/45/3/1520-0469_1988_045_0463_atfsll_2_0_co_2.xml)
- Satoh, M., T. Inoue, and H. Miura, 2010: Evaluations of cloud properties of global and local cloud system resolving models using calipso and cloudsat simulators. *Aerosol and Clouds*, **115**, doi:10.1029/2009JD012247.  
 URL <https://agupubs.onlinelibrary.wiley.com/doi/full/10.1029/2009JD012247>
- Schumacher, R. S., A. J. Clark, M. Xue, and F. Kong, 2013: Factors influencing the development and maintenance of nocturnal heavy-rain-producing convective systems in a storm-scale ensemble. *Monthly Weather Review*, **141**, 2778–2801, doi:10.1175/MWR-D-12-00239.1.  
 URL <https://journals.ametsoc.org/view/journals/mwre/141/8/mwr-d-12-00239.1.xml#bib14>
- Schumacher, R. S. and R. H. Johnson, 2008: Mesoscale processes contributing to extreme rainfall in a midlatitude warm-season flash flood. *Monthly Weather Review*, **136**, 3964–3986, doi:10.1175/2008MWR2471.1.  
 URL <https://journals.ametsoc.org/view/journals/mwre/136/10/2008mwr2471.1.xml>
- 2009: Quasi-stationary, extreme-rain-producing convective systems associated with midlevel cyclonic circulations. *Weather and Forecasting*, **24**, 555–574, doi:10.1175/2008WAF2222173.1.  
 URL [https://journals.ametsoc.org/view/journals/wefo/24/2/2008waf2222173\\_1.xml?tab\\_body=fulltext-display#i1520-0434-24-2-555-f07](https://journals.ametsoc.org/view/journals/wefo/24/2/2008waf2222173_1.xml?tab_body=fulltext-display#i1520-0434-24-2-555-f07)

Schwartz, C. S., G. S. Romine, M. L. Weisman, R. A. Sobash, K. R. Fossell, K. W. Manning, , and S. B. Trier, 2015: A real-time convection-allowing ensemble prediction system initialized by mesoscale ensemble kalman filter analyses. *Weather and Forecasting*, **30**, 1158–1181, doi:10.1175/WAF-D-15-0013.1.  
URL [https://journals.ametsoc.org/view/journals/wefo/30/5/waf-d-15-0013\\_1.xml](https://journals.ametsoc.org/view/journals/wefo/30/5/waf-d-15-0013_1.xml)

Scorer, R. S., 1957: Experiments on convection of isolated masses of buoyant fluid. **2**, 583–594, doi:10.1017/S0022112057000397.  
URL <https://www.cambridge.org/core/journals/journal-of-fluid-mechanics/article/abs/experiments-on-convection-of-isolated-B56D544C7DB9E91660BAAC3498569ABE>

Sherburn, K. D. and M. D. Parker, 2014: Climatology and ingredients of significant severe convection in high-shear, low-cape environments. *Weather and Forecasting*, **29**, 854–877, doi:10.1175/WAF-D-13-00041.1.  
URL [https://journals.ametsoc.org/view/journals/wefo/29/4/waf-d-13-00041\\_1.xml#bib24](https://journals.ametsoc.org/view/journals/wefo/29/4/waf-d-13-00041_1.xml#bib24)

Skamarock, W., J. Klemp, J. Dudhia, D. Gill, D. Barker, W. Wang, and J. Powers, 2005: A description of the advanced research wrf version 2. doi:10.5065/D68S4MVH.  
URL <https://journals.ametsoc.org/view/journals/mwre/137/7/2009mwr2645.1.xml>

Trier, S. B. and C. A. Davis, 2002: Influence of balanced motions on heavy precipitation within a long-lived convectively generated vortex. *Monthly Weather Review*, **130**, 877–899, doi:10.1175/1520-0493(2002)130<0877:IOBMOH>2.0.CO;2.  
URL [https://journals.ametsoc.org/view/journals/mwre/130/4/1520-0493\\_2002\\_130\\_0877\\_iobmoh\\_2.0.co\\_2.xml](https://journals.ametsoc.org/view/journals/mwre/130/4/1520-0493_2002_130_0877_iobmoh_2.0.co_2.xml)

Trigg, M. A., C. E. Birch, J. C. Neal, P. D. Bates2, A. Smith, C. C. Sampson, D. Yamazaki, Y. Hirabayashi, F. Pappenberger, and E. Dutra, 2016: The credibility challenge for global fluvial flood risk analysis. *Environ. Res. Lett.*, **11**, doi:10.1088/1748-9326/11/9/094014.  
URL <https://iopscience.iop.org/article/10.1088/1748-9326/11/9/094014/meta>

Weisman, M. L., C. Evans, and L. Bosart, 2013: The 8 may 2009 superderecho: Analysis of a real-time explicit convective forecast. *Weather and Forecasting*, **28**, 863–892, doi:10.1175/WAF-D-12-00023.1.  
URL [https://journals.ametsoc.org/view/journals/wefo/28/3/waf-d-12-00023\\_1.xml](https://journals.ametsoc.org/view/journals/wefo/28/3/waf-d-12-00023_1.xml)

Weng, Y. and F. Zhang, 2012a: Advances in convection-permitting tropical cyclone analysis and prediction through enkf assimilation of reconnaissance aircraft observations.

- Journal of the Meteorological Society of Japan*, **94**, 345–358, doi:10.2151/jmsj.2016-018.  
 URL [https://www.jstage.jst.go.jp/article/jmsj/94/4/94\\_2016-018/\\_article](https://www.jstage.jst.go.jp/article/jmsj/94/4/94_2016-018/_article)
- 2012b: Assimilating airborne doppler radar observations with an ensemble kalman filter for convection-permitting hurricane initialization and prediction: Katrina (2005). *Monthly Weather Review*, **140**, 841–859, doi:10.1175/2011MWR3602.1.  
 URL <https://journals.ametsoc.org/view/journals/mwre/140/3/2011mwr3602.1.xml>
- Wheatley, D. M., K. H. Knopfmeier, T. A. Jones, and G. J. Creager, 2015: Storm-scale data assimilation and ensemble forecasting with the nssl experimental warn-on-forecast system. part i: Radar data experiments. *Weather and Forecasting*, **30**, 1795–1817, doi:10.1175/WAF-D-15-0043.1.  
 URL [https://journals.ametsoc.org/view/journals/wefo/30/6/waf-d-15-0043\\_1.xml#bib26](https://journals.ametsoc.org/view/journals/wefo/30/6/waf-d-15-0043_1.xml#bib26)
- Whitaker, J. S. and T. M. Hamill, 2002: Ensemble data assimilation without perturbed observations. *Monthly Weather Review*, **130**, 1913–1924, doi:10.1175/1520-0493(2002)130<1913:EDAWPO>2.0.CO;2.  
 URL [https://journals.ametsoc.org/view/journals/mwre/130/7/1520-0493\\_2002\\_130\\_1913\\_edawpo\\_2.0.co\\_2.xml](https://journals.ametsoc.org/view/journals/mwre/130/7/1520-0493_2002_130_1913_edawpo_2.0.co_2.xml)
- Williams, E. and N. Renno, 1993: An analysis of the conditional instability of the tropical atmosphere. *Monthly Weather Review*, **121**, 21–36, doi:10.1175/1520-0493(1993)121<0021:AAOTCI>2.0.CO;2.  
 URL [https://journals.ametsoc.org/view/journals/mwre/121/1/1520-0493\\_1993\\_121\\_0021\\_aaotci\\_2\\_0\\_co\\_2.xml](https://journals.ametsoc.org/view/journals/mwre/121/1/1520-0493_1993_121_0021_aaotci_2_0_co_2.xml)
- Wing, O. E. J., P. D. Bates, A. M. Smith, C. C. Sampson, K. A. Johnson, J. Fargione, and P. Morefield, 2018: Estimates of present and future flood risk in the conterminous united states. *Environ. Res. Lett.*, **13**, 104–118, doi:10.1088/1748-9326/aaac65.  
 URL <https://iopscience.iop.org/article/10.1088/1748-9326/aaac65>
- Yang, F., D. Cerrai, and E. N. Anagnostou, 2021: The effect of lead-time weather forecast uncertainty on outage prediction modeling. *Forecasting*, **3**, 501–516, doi:10.3390/forecast3030031.  
 URL <https://www.mdpi.com/2571-9394/3/3/31>
- Yuter, S. E. and R. A. Houze, 1995: Three-dimensional kinematic and microphysical evolution of florida cumulonimbus. part ii: Frequency distributions of vertical velocity, reflectivity, and differential reflectivity. *Monthly Weather Review*, **123**, 1941 – 1963, doi:10.1175/1520-0493(1995)123<1941:TDKAME>2.0.CO;2.

- URL [https://journals.ametsoc.org/view/journals/mwre/123/7/1520-0493\\_1995\\_123\\_1941\\_tdkame\\_2\\_0\\_co\\_2.xml](https://journals.ametsoc.org/view/journals/mwre/123/7/1520-0493_1995_123_1941_tdkame_2_0_co_2.xml)
- Zhang, C., Y. Wang, and K. Hamilton, 2011a: Improved representation of boundary layer clouds over the southeast pacific in arw-wrf using a modified tiedtke cumulus parameterization scheme. *Monthly Weather Review*, **139**, 3489–3513, doi:10.1175/MWR-D-10-05091.1.  
URL <https://journals.ametsoc.org/view/journals/mwre/139/11/mwr-d-10-05091.1.xml>
- Zhang, D.-L. and J. M. Fritsch, 1987: Numerical simulation of the meso- scale structure and evolution of the 1977 johnstown flood. part ii: Inertially stable warm-core vortex and the mesoscale convective complex. *Journal of the Atmospheric Sciences*, **44**, 2593–2612, doi:10.1175/1520-0469(1987)044<2593:NSOTMS>2.0.CO;2.  
URL [https://journals.ametsoc.org/view/journals/atsc/44/18/1520-0469\\_1987\\_044\\_2593\\_nsotms\\_2\\_0\\_co\\_2.xml](https://journals.ametsoc.org/view/journals/atsc/44/18/1520-0469_1987_044_2593_nsotms_2_0_co_2.xml)
- Zhang, F., M. Minamide, and E. E. Clothiaux, 2016a: Potential impacts of assimilating all-sky infrared satellite radiances from goes-r on convection-permitting analysis and prediction of tropical cyclones. *AGU Advances*, **43**, doi:10.1002/2016GL068468.  
URL <https://agupubs.onlinelibrary.wiley.com/doi/10.1002/2016gl068468>
- Zhang, F. and Y. Weng, 2015: Predicting hurricane intensity and associated hazards: A five-year real-time forecast experiment with assimilation of airborne doppler radar observations. *Bulletin of the American Meteorological Society*, **96**, 25–33, doi:10.1175/BAMS-D-13-00231.1.  
URL <https://journals.ametsoc.org/view/journals/bams/96/1/bams-d-13-00231.1.xml>
- Zhang, F., Y. Weng, J. F. Gamache, and F. D. Marks, 2011b: Performance of convection-permitting hurricane initialization and prediction during 2008–2010 with ensemble data assimilation of inner-core airborne doppler radar observations. *AGU Advances*, **38**, doi:10.1029/2011GL048469.  
URL <https://agupubs.onlinelibrary.wiley.com/doi/10.1029/2011gl048469>
- Zhang, F., Y. Weng, J. A. Sippel, Z. Meng, and C. H. Bishop, 2009: Cloud-resolving hurricane initialization and prediction through assimilation of doppler radar observations with an ensemble kalman filter. *Monthly Weather Review*, **137**, 2105–2125, doi:10.1175/2009MWR2645.1.  
URL <https://journals.ametsoc.org/view/journals/mwre/137/7/2009mwr2645.1.xml>

- Zhang, J., K. Howard, C. Langston, B. Kaney, Y. Qi, L. Tang, H. Grams, Y. Wang, S. Cocks, S. Martinaitis, A. Arthur, K. Cooper, J. Brogden, and D. Kitzmiller, 2016b: Multi-radar multi-sensor (mrms) quantitative precipitation estimation: Initial operating capabilities. *Bulletin of the American Meteorological Society*, **97**, 621–638, doi:10.1175/BAMS-D-14-00174.1.  
URL <https://journals.ametsoc.org/view/journals/bams/97/4/bams-d-14-00174.1.xml>
- Zhang, Y., X. Chen, and M. M. Bell, 2023: Improving short-term qpf using geostationary satellite all-sky infrared radiances: Real-time ensemble data assimilation and forecast during the precip 2020 and 2021 experiments. *Weather and Forecasting*, **38**, 591–609, doi:10.1175/WAF-D-22-0156.1.  
URL <https://journals.ametsoc.org/view/journals/wefo/38/4/WAF-D-22-0156.1.xml>
- Zhang, Y., S. B. Sieron, Y. Lu, X. Chen, R. G. Nystrom, M. Minamide, M.-Y. Chan, C. M. Hartman, Z. Yao, J. H. R. Jr., A. Okazaki, S. J. Greybush, E. E. Clothiaux, and F. Zhang, 2021: Ensemble-based assimilation of satellite all-sky microwave radiances improves intensity and rainfall predictions for hurricane harvey (2017). *AGU Advances*, **48**, doi:10.1029/2021GL096410.  
URL <https://agupubs.onlinelibrary.wiley.com/doi/full/10.1029/2021GL096410>
- Zhou, L. S.-J. C. J.-H. H. L. M. C. X. . R. S. L., L., 2019: Toward convective-scale prediction within the next generation global prediction system. *Bulletin of the American Meteorological Society*, **100**, 1225–1243, doi:10.1175/BAMS-D-17-0246.1.  
URL <https://journals.ametsoc.org/view/journals/bams/100/7/bams-d-17-0246.1.xml>
- Zipser, E. J., 1977: Mesoscale and convective-scale downdrafts as distinct components of squall-line structure. *Monthly Weather Review*, **105**, 1568–1589, doi:10.1175/1520-0493(1977)105<1568:MACDAD>2.0.CO;2.  
URL [https://journals.ametsoc.org/view/journals/mwre/105/12/1520-0493\\_1977\\_105\\_1568\\_macdad\\_2\\_0\\_co\\_2.xml](https://journals.ametsoc.org/view/journals/mwre/105/12/1520-0493_1977_105_1568_macdad_2_0_co_2.xml)